Trace element composition of iron oxides from IOCG and IOA deposits: relationship to hydrothermal alteration and deposit subtypes — Source link ↗

Xiao-Wen Huang, Xiao-Wen Huang, Emilie Boutroy, Sheida Makvandi ...+3 more authors

Institutions: Laval University, Chinese Academy of Sciences, Geological Survey of Canada

Topics: Iron oxide, Iron oxide copper gold ore deposits, Mineral redox buffer, Hematite and Magnetite

Related papers:

- Discriminant diagrams for iron oxide trace element fingerprinting of mineral deposit types

- The chemistry of hydrothermal magnetite: A review

- Trace elements in magnetite as petrogenetic indicators

- Variation in trace element content of magnetite crystallized from a fractionating sulfide liquid, Sudbury, Canada: Implications for provenance discrimination

- Trace elements in magnetite from massive iron oxide-apatite deposits indicate a combined formation by igneous and magmatic-hydrothermal processes

1 Trace element composition of iron oxides from IOCG and IOA deposits:

2 Relationship to hydrothermal alteration and deposit subtypes

3 Xiao-Wen Huang[1,2,3,†] , Émilie Boutroy[2,4] , Sheida Makvandi[2,3] , Georges Beaudoin[2,3] ,

4 Louise Corriveau[5] , Anthony Franco De Toni[6]

5

6 [1]State Key Laboratory of Ore Deposit Geochemistry, Institute of Geochemistry,

7 Chinese Academy of Sciences, Guiyang 550081, China

8 [2]Département de géologie et de génie géologique, Université Laval, Québec, QC G1V

9 0A6, Canada

10 [3]Research Center on the Geology and Engineering of Mineral Resources (E4m),

11 Université Laval, Québec, QC G1V 0A6, Canada

12 [4]Agnico Eagle Mines Limited, 1655 3e Av, Val d'Or, QC J9P 1W1, Canada

13 [5]Geological Survey of Canada, Natural Resources Canada, 490 rue de la Couronne,

14 Québec, QC G1K9A9, Canada

15 [6]SOQUEM inc., 1740 chemin Sullivan, suite 2000, Val-d'Or, QC, J9P 7H1, Canada

16

17 [†]Corresponding author: e-mail, huangxiaowen2008@live.cn

18

19

20

21

22

23 **Abstract**

24 Trace element compositions of magnetite and hematite from sixteen well-studied iron

25 oxide–copper–gold (IOCG) and iron oxide apatite (IOA) deposits, combined with

26 partial least squares-discriminant analysis (PLS-DA), were used to investigate the

27 factors controlling the iron oxide chemistry and the links between the chemical

28 composition of iron oxides and hydrothermal processes, as divided by alteration types

29 and IOCG and IOA deposit subtypes. Chemical compositions of iron oxides are

30 controlled by oxygen fugacity, temperature, co-precipitating sulfides, and host rocks.

31 Iron oxides from hematite IOCG deposits show relatively high Nb, Cu, Mo, W, and

32 Sn contents, and can be discriminated from those from magnetite + hematite and

33 magnetite IOA deposits. Magnetite IOCG deposits show a compositional diversity

34 and overlap with the three other types, which may be due to the incremental

35 development of high-temperature Ca-Fe and K-Fe alteration. Iron oxides from the

36 high-temperature Ca-Fe alteration can be discriminated from those from high- and

37 low-temperature K-Fe alteration by higher Mg and V contents. Iron oxides from

38 low-temperature K-Fe alteration can be discriminated from those from

39 high-temperature K-Fe alteration by higher Si, Ca, Zr, W, Nb, and Mo contents. Iron

40 oxides from IOA deposits can be discriminated from those from IOCG deposits by

41 higher Mg, Ti, V, Pb, and Sc contents. The composition of IOCG and IOA iron oxides

42 can be discriminated from those from porphyry Cu, Ni-Cu, and volcanogenic massive

43 sulfide deposits.

44 **Keywords:** Trace elements, iron oxides, deposit subtypes, alteration types,

45   discrimination diagram

46

Introduction

48   The iron oxides, including magnetite and hematite, are common major or accessory

49   minerals in igneous, sedimentary, and metamorphic rocks, and in various types of

50   mineral deposits (Ramdohr 1980; Dupuis and Beaudoin 2011). A range of minor and

51   trace elements such as Al, Ti, Mg, Mn, Zn, Cr, V, Ni, Co and Ga can be incorporated

52   into the inverse spinel structure of magnetite (Buddington and Lindsley 1964; Frost

53   and Lindsley 1991; Dupuis and Beaudoin 2011; Nadoll et al. 2014). Trace elements in

54   magnetite have been used as provenance indicators of sediments (Grigsby 1990;

55   Razjigaeva and Naumova 1992; Makvandi et al. 2015), petrogenetic indicators

56   (Barnes and Roeder 2001; Dare et al. 2014), and as mineral exploration tools (Dupuis

57   and Beaudoin 2011; Boutroy et al. 2014; Sappin et al. 2014; Makvandi et al. 2015,

58   2016a, b). They are also widely used to fingerprint various deposit types or

59   ore-forming processes (Müller et al. 2003; Carew 2004; Singoyi et al. 2006; Rusk et

60   al. 2009; Beaudoin and Dupuis 2010; Dupuis and Beaudoin 2011; Dare et al. 2012;

61   Nadoll et al. 2012; Huang et al. 2013, 2015a, b, 2016; Chen et al. 2015; Knipping et al.

62   2015b; Liu et al. 2015).

63   The composition of magnetite and hematite is controlled by (1) the composition of

64   magma (Dare et al. 2012, 2014; Liu et al., 2015), or composition of hydrothermal

65   solutions which is determined by the composition of source rocks and fluid-rock

66   interactions along the flow path (Carew 2004; Dare et al. 2012, 2014; Nadoll et al.

67 2014; Huang et al. 2016), (2) the physical and chemical conditions that influence the

68 partition coefficients of elements, such as temperature, pressure, rate of cooling,

69 oxygen fugacity, silica activity (Goldschmidt 1958; Buddington and Lindsley 1964;

70 Fleet 1981; Wechsler et al. 1984; Whalen and Chappell 1988; Ghiorso and Sack 1991;

71 Righter et al. 2006; Sievwright et al. 2017), and (3) the co-crystallization minerals

72 during which some specific elements may compete with magnetite and hematite

73 (Carew 2004; Dare et al. 2012; Huang et al. 2014; Nadoll et al. 2014).

74 The iron oxide–copper–gold (IOCG) deposit class has attracted growing

75 exploration and research interest since the discovery of the giant Olympic Dam

76 deposit (Hitzman et al. 1992). IOCG deposits are characterized by Cu-sulfides $\pm$ Au

77 hydrothermal mineralization with abundant magnetite or hematite. They occur in

78 rocks ranging in age from the Late Archean to the Mesozoic (Williams et al. 2005).

79 These deposits show a great variation in geological settings, alteration systematics as

80 well as mineralizing fluid compositions (Hitzman et al. 1992; Hitzman 2000; Sillitoe

81 2003; Williams et al. 2005). Iron oxide apatite (IOA) deposits are characterized by

82 apatite-bearing iron ores lacking copper, gold and polymetallic mineralization beyond

83 rare-earth elements (Williams 2010a). The IOA deposits studied are also referred to

84 Kiruna-type IOA deposits that are characterized by Ti-poor magnetite. IOCG and IOA

85 deposits can be subdivided into hematite, hematite + magnetite, and magnetite groups

86 based on the principal iron oxide (Williams 2010a). Magnetite-group and

87 hematite-group IOCG deposits form in a variety of hydrothermal environments,

88 across distinct temperature ranges and fluid evolution processes (Skirrow 2010;

4

89   Williams 2010b). Magnetite-group IOCG deposits represent the higher temperature

90   part of the IOCG spectrum contrasting with hematite-group deposits, such as Olympic

91   Dam, that are characterized by lower temperature hematite and white mica-dominated

92   alteration (Williams 2010a). IOA deposits characterize a number of regions

93   worldwide where they generally display an association with calc-alkaline arc

94   magmatism (Barton and Johnson 1996; Williams et al. 2005). Both magnetite-group

95   and magnetite + hematite-group IOA deposits are commonly enveloped by breccias

96   with magnetite ± hematite ± actinolite matrix that occur within large scale Na ± Ca

97   and high-temperature Ca-Fe alteration systems (Corriveau et al. 2010, 2016; Williams

98   2010a; Tornos et al. 2016).

99   Both IOCG and IOA deposits are closely associated with extensive hydrothermal

100   alteration, divided into Na to Na-Ca alteration, high-temperature Ca-Fe,

101   high-temperature K-Fe, and low-temperature K-Fe and Ca-Mg alteration types

102   (Corriveau et al. 2010, 2016). Different alteration stages have characteristic mineral

103   assemblages, chemical footprints and signatures, metal associations, formation

104   temperature, and fluid composition (Corriveau et al. 2010, 2016; Montreuil et al. 2013,

105   2016).

106   Different classification schemes of iron oxides from IOCG and IOA deposits have

107   been proposed based on trace element composition of iron oxides. Dupuis and

108   Beaudoin (2011) have proposed the Ca+Al+Mn vs. Ti+V and Ni/(Cr+Mn) vs. Ti+V

109   diagrams to discriminate IOCG and IOA deposits from Fe-Ti-V, porphyry, skarn

110   deposits, and banded iron formation (BIF). In these diagrams, iron oxides from IOCG

111 deposits can be separated from those from IOA deposits due to lower total Ti and V

112 contents. Knipping et al. (2015b) used a plot of V vs. Cr to distinguish IOA deposits

113 from magmatic Fe-Ti-V, porphyry, and IOCG deposits, on the basis that IOA deposits

114 magnetite has lower Cr, but higher V, concentrations than IOCG deposits. Heidarian

115 et al. (2016) and Broughm et al. (2017) demonstrated that the V vs. Ti, V vs. Ni+Co,

116 V vs. Ni, and V/Ti vs. Ni/Ti diagrams, proposed by Loberg and Horndahl (1983),

117 were useful to discriminate IOA deposits from magmatic Fe-Ti deposits and BIF.

118 Despite the successful application of these diagrams, all of them have limitations with

119 significant overlaps (e.g., Broughm et al. 2017). Binary score plots based on partial

120 least squares-discriminant analysis (PLS-DA) proved to be efficient in separating

121 IOCG and IOA deposits from porphyry, Ni-Cu, VMS deposits, and VMS-related BIF

122 (Makvandi et al. 2016b). PLS-DA showed that magnetite from IOCG deposits is

123 characterized higher Si, whereas magnetite from IOA deposits has higher Ti and Co

124 concentrations (Makvandi et al. 2016b).

125 In this paper, we selected nine IOCG and seven IOA deposits representing major

126 examples of both deposits, and their related alteration types (Fig. 1, Online Resource

127 1; Williams et al. 2005). These deposits formed in a range of geological environments

128 with different ages, host rocks, and alteration assemblages, which are considered

129 representative for both types of mineral deposits. By investigating the mineral

130 paragenesis with emphasis on magnetite and/or hematite associated with

131 mineralization, trace element composition of magnetite and hematite were determined

132 by electron probe microanalyzer (EPMA) and laser ablation-inductively coupled

133 plasma-mass spectrometry (LA-ICP-MS). Based on these petrographic and

134 geochemical analyses, we discuss the factors controlling the iron oxide chemistry and

135 the links between the chemical composition of iron oxides and hydrothermal

136 processes, as divided by alteration types and deposit subtypes.

137

Sample selection and classification

Sample selection

140 IOCG deposits include Igarapé Bahia, Alemao, Sossego, Alvo 118, and Salobo from

141 the Carajas district in Brazil, Olympic Dam and Ernest Henry from the Gawler craton

142 and the Cloncurry district, respectively, in Australia, Candelaria from the Central

143 Andes district in Chile, and Kwyjibo from the Grenville Province in Canada (Fig. 1

144 and Online Resource 1). IOA deposits include Kiruna (or Kiirunavaara) and Rektorn

145 from the Norrbotten district of northern Sweden, El Romeral from the Central Andes

146 in Chile, Savage River from the Arthur Lineament in Australia, Pilot Knob and Pea

147 Ridge from the Missouri district in the USA, and Lyon Mountain from the Grenville

148 Province in USA (Fig. 1 and Online Resource 1). For each deposit studied, between

149 one to ten polished sections or polished thin sections sampled from ore zones have

150 been used, from which three to four magnetite and/or hematite grains have been

151 analyzed by at least three spots per grain with the EPMA. The selected grains are in

152 equilibrium with other mineral grains in order to avoid elemental exchange after their

153 formation. Iron oxide grains with reequilibration textures (Hu et al. 2015; Huang et al.

154 2018) are excluded because the chemical composition of these grains may have been

155   modified during replacement. Selected larger grains were also analyzed by

156   LA-ICP-MS.

157

158   **Sample classification**

159   Deposit subtypes

160   Williams (2010a) suggested that IOCG and IOA deposits can be subdivided into

161   hematite, hematite + magnetite, and magnetite groups based on the nature of the

162   principal iron oxides present. Each of these groups includes a number of different

163   deposit subtypes that exhibit significantly different physical property distributions

164   (e.g., density, remanence, conductivity, radiometric K and U). According to the type

165   of major iron oxides, the deposits are divided into magnetite-group IOCG deposits,

166   hematite-group IOCG deposit, magnetite-group IOA deposits, and magnetite +

167   hematite-group IOA deposits (Online Resource 1).

168

169   Alteration types

170   Corriveau et al. (2010, 2016) proposed an alteration zoning model that frames the

171   evolution of iron oxide and alkali-calcic hydrothermal systems and their iron

172   oxide-apatite and magnetite- and hematite-group IOCG deposits. They defined five

173   main alteration stages, reflecting declining temperature and increasing oxygen

174   fugacity. The main alteration types are Na, high-temperature Ca-Fe, high-temperature

175   K-Fe, low-temperature and hydrolytic K-Fe as well as transitional Na-Ca-Fe, skarn,

176   potassic felsite, potassic skarn and low-temperature Ca-Mg alteration.

177   Early Na (± Ca) and high-temperature Ca-Fe (± Na) alteration zones are commonly

178   laterally extensive, regional in scale and commonly lack polymetallic mineralization

179   unless replaced by fertile K-Fe alteration types. Sodic alteration principally results in

180   albitite, which generally contains variable amounts of scapolite and cryptocrystalline

181   quartz (Corriveau et al. 2016). The Ca-Fe alteration consists of variable proportions of

182   amphibole (actinolite or hornblende) and magnetite as well as accessory apatite,

183   garnet, and clinopyroxene. With garnet and clinopyroxene, epidote is commonly part

184   of earlier skarn assemblages formed after, or coeval, with albitization and

185   subsequently incrementally replaced by amphibole during high-temperature Ca-Fe

186   alteration. The high-temperature K-Fe alteration consists of variable proportions of

187   K-feldspar, magnetite, and biotite, whereas the low-temperature K-Fe alteration

188   consists of hematite, chlorite, K-feldspar, white mica (sericite), carbonates, and quartz.

189   All the samples were classified according to the alteration type that hosts the IOCG or

190   IOA mineralization based on the mineral assemblages observed in thin sections and

191   alteration description in literature (Online Resource 2).

192

193   **Methodology**

194   **Analytical methods**

195   EPMA analyses

196   Major and minor/trace elements in iron oxides were analyzed at Université Laval

197   using a CAMECA SX-100 EPMA, equipped with five wavelength-dispersive

198   spectrometers, using a 10-μm diameter beam with a voltage of 15 kV and a current of

199 100 nA. Minor and trace elements K, Ca, Al, Si, Ti, Mg, Mn, Cr, V, Sn, Cu, Zn, and

200 Ni, typically have element concentrations commonly above the detection limit.

201 Analytical conditions are similar to those described by Boutroy et al. (2014).

202 Calibration was achieved using a range of natural and synthetic standards, comprising

203 simple oxides (GEO Standard Block of P and H Developments) and natural minerals

204 (Mineral Standard Mount MINM 25–53, Astimex Scientific) (Jarosewich et al. 1980).

205 The background was measured on one side of the peak for 15-20 s at a position free of

206 interfering element X-ray and the concentration was counted over the peak for 20 to

207 40 s depending on the element. Detection limits are ~100 ppm for Zn, ~80 ppm for Cu,

208 ~60 ppm for Ni, 40-50 ppm for V, Cr, Mn, Sn, and 15-25 ppm for K, Ca, Ti, Al, Si,

209 and Mg (Online Resource 3).

210

211 LA-ICP-MS analyses

212 Iron oxides were analyzed by using a RESOlution M-50 193 nm Excimer Laser

213 Ablation system coupled with an Agilent 7700x ICP-MS at Université du Québec à

214 Chicoutimi (UQAC), using a beam size of 25 to 80 µm with a speed stage of 3 to 15

215 µm/s and a laser frequency of 10 Hz and a power of 5 mJ per pulse. The minor and

216 trace elements ^{24}Mg, ^{27}Al, ^{45}Sc, ^{47}Ti, ^{51}V, ^{52}Cr, ^{55}Mn, ^{60}Ni, ^{66}Zn, ^{75}As, ^{59}Co, $^{69,\,71}$Ga,

217 ^{74}Ge, ^{89}Y, $^{90,\,92}$Zr, ^{95}Mo, ^{101}Ru, ^{105}Pd, ^{111}Cd, ^{118}Sn, ^{121}Sb, ^{93}Nb, ^{107}Ag, ^{115}In, ^{178}Hf, ^{181}Ta,

218 ^{182}W, ^{187}Re, ^{193}Ir, ^{195}Pt, ^{197}Au, ^{208}Pb and ^{209}Bi were measured. Sulfur, Si, Ca and Cu

219 were monitored to detect mineral inclusions. Multiple isotopes of Zr and Ga were

220 measured to resolve isobaric interferences. Analytical conditions are similar to those

221 described by Boutroy et al. (2014). A single Fe-rich reference material, GSE-1G

222 containing all the required elements, was used for calibration (Savard et al. 2012). To

223 monitor the quality of the analyses, reference materials GSD-1G and BC28 (natural

224 magmatic magnetite) were routinely analyzed. Data reduction was carried out using

225 the software Iolite. Lines were ablated across the width of a magnetite grain for a

226 period ranging from 20 to 60 seconds depending on the grain size, after monitoring a

227 gas blank for 20–30 seconds. Iron was used as the internal standard to compute

228 concentration assuming stoichiometric magnetite (Dare et al. 2012). Detection limits

229 are 0.01 to 0.02 ppm for ^{24}Mg, ^{59}Co, ^{89}Y, $^{90.92}$Zr, ^{93}Nb, ^{101}Ru, ^{105}Pd, ^{107}Ag, ^{115}In, ^{181}Ta,

230 ^{182}W, ^{187}Re, ^{197}Au, ^{208}Pb, ^{209}Bi; 0.025 to 0.05 ppm for ^{45}Sc, ^{51}V, ^{95}Mo, ^{178}Hf; 0.055 to

231 0.1 ppm for ^{65}Cu, ^{71}Ga, ^{111}Cd, ^{121}Sb, ^{193}Ir, ^{195}Pt; 0.1 to 0.5 ppm for ^{27}Al, ^{47}Ti, ^{60}Ni,

232 ^{66}Zn, ^{74}Ge, ^{75}As, ^{118}Sn; 0.55 to 1 ppm for ^{52}Cr and ^{55}Mn (Online Resource 4).

233

234 **Statistical methods**

235 Estimation of average composition

236 Electron microprobe and LA-ICP-MS datasets are typically censored because they

237 contain non-detects that are below the computed minimum detection limits (Helsel

238 2005). The average composition of iron oxides is estimated using the nonparametric

239 Kaplan-Meier (K-M) method (NADA package in R; Lee and Helsel 2007).

240

241 Data preprocessing and partial least squares-discriminant analysis

242 In order to investigate the possible factors controlling the variations of trace element

11

243 composition of iron oxides and unravel the relationships between iron oxide

244 chemistry and host rocks, alteration and deposit types, the individual EPMA and

245 LA-ICP-MS analyses were investigated by partial least squares-discriminant analysis

246 (PLS-DA). PLS-DA can also identify discriminant elements separating different

247 sample classes based on iron oxide compositions. Seven of thirteen elements analyzed

248 by EPMA are investigated by PLS-DA, whereas K, Sn, Cu, Zn, Ni, and Cr were

249 excluded because the dataset contains more than 40% censored data. According to this

250 criterion, Y, P, Ta, and Hf, analyzed by LA-ICP-MS, are not considered for PLS-DA.

251 Censored compositional data were imputed using the k-nearest neighbors function

252 with the Aitchison distance (robCompositions package in R; Hron et al. 2010;

253 Makvandi et al. 2016b). Geochemical data, summed to 100%, can lead to spurious

254 correlations when studying co-variations (Aitchison 1986; Whitten 1995). This is

255 referred as the 'closure problem', inherent to all compositional datasets (Aitchison

256 1986). In this study, data were transformed using centered-log ratio (clr) method

257 (Thió-Henestrosa and Martín-Fernández 2005) that is a suitable method for

258 multivariate statistical techniques such as PLS-DA (Aitchison 1986; Egozcue et al.

259 2003; Makvandi et al. 2016b).

260 Statistical analysis was carried out using PLS-DA method as described in

261 Makvandi et al. (2016b). PLS-DA is a supervised classification technique using

262 labeled data, which sharpens the separation between groups of observations by

263 rotating principal components, and results in the maximum separation among classes

264 and the identification of the variables responsible for the separation of different

265   classes (De Iorio et al. 2008). In the PLS-DA method, a series of orthogonal

266   components (latent variables) are extracted to relate the X (N × K) and Y (N × M)

267   matrices by maximizing the covariance between the two matrices using the following

268   equations (Wold et al. 2001; Eriksson et al., 2013; Brereton and Lloyd 2014):

269    $X = TP^T + E$ (1)

270    $Y = TQ^T + F$ (2)

271    $T = XW^*$ (3)

272   where T (N × r) is the score matrix containing r orthogonal PLS components (scores).

273   The T matrix represents the common latent variable space of both X and Y matrices.

274   For Eqs. (1)–(3), P (N × r) and Q (M × r) are the loadings matrices for X and Y,

275   respectively. The weight matrix (W*) consists of the coefficients of the linear

276   combinations of the X variables that are the most predictive of Y, whereas E and F are

277   the model residuals.

278   Following Makvandi et al. (2016b), loadings and weights biplots (qw^*_1-qw^*_2),

279   score scatter plots (t_1-t_2), score contribution plots, and variable importance on

280   projection (VIP) plots were generated for different datasets. Loadings biplots indicate

281   the correlation among different variables (elements), and the relationship between the

282   variables and different sample classes (e.g., host rock/deposit type/alteration type).

283   The loading values show the impact of elements on the model, and the sign of the

284   values indicates the positive or negative correlation between the elements. As a result,

285   elements that plot in the vicinity of each other in the PLS-DA loadings space show

286   strong positive correlations, and they are negatively correlated to those in an opposite

287   quadrant. The correlation among variables and sample classes control the distribution

288   of samples in the score scatter plots. Score contribution plots depict the compositional

289   differences between the mean composition of a cluster (sample group) and the mean

290   composition of the whole dataset. Given that data is mean-centered prior to PLS-DA,

291   the origin of score scatter plots represents the mean composition of the whole dataset

292   (Makvandi et al. 2016b). The VIP plots are also used to indicate the impact of

293   different variables on the sample classification, where VIP values equal and/or larger

294   than 1 are the most important in the classification (Eriksson et al. 2013).

295

Results

297   **Petrography of mineralization and alteration**

298   The mineral assemblages of each thin section are characterized by macroscopic and

299   microscopic observation (Online Resource 2). Combined with the description of

300   hydrothermal alteration in each deposit, the mineral assemblages in thin section are

301   used to define deposit subtypes and alteration types.

302   *Igarapé Bahia:* The main iron oxide in the Igarapé Bahia Cu-Au deposit is

303   magnetite (Fig. 2a), and thus this deposit is classified into magnetite-group IOCG

304   deposits. The hydrothermal alteration and mineralization at this deposit is

305   characterized by (1) Fe metasomatism leading to the formation of grunerite, fayalite,

306   and/or Fe oxides (magnetite and/or hematite), (2) carbonate alteration (mainly

307   siderite), (3) chalcopyrite and bornite, (4) quartz-poor gangue, (5) low REE, and (6)

308   enrichment in U and Co from early to late (Tazava and De Oliveira 2000; Tallarico et

309　al. 2005; Dreher et al. 2008). Three samples from this deposit have similar mineral

310　assemblages of magnetite, chalcopyrite, and siderite (Fig. 2a), which is typical of Fe

311　metasomatism. Magnetite is subhedral to euhedral with grain size from a few microns

312　to ~300 µm (Fig. 2a). The primary Cu-Au mineralization in Igarapé Bahia is closely

313　related to Fe chlorite, siderite, and magnetite-rich breccias (Tallarico et al. 2005).

314　Magnetite breccias exhibit a granular matrix of euhedral magnetite cemented by

315　chalcopyrite and bornite, together with minor grunerite, actinolite, minnesotaite,

316　biotite, stilpnomelane, K-feldspar, tourmaline, fluorite, siderite, ankerite, and uraninite

317　(Tallarico et al. 2005). This mineral assemblage defines a distinctive K-Fe–enriched

318　zone in the deposit (Tallarico et al. 2005), belonging to the high-temperature K-Fe

319　alteration facies.

320　　*Alemao:* The main iron oxide in the Alemao Cu-Au deposit is magnetite (Fig. 2b),

321　which defines this deposit as a magnetite-group IOCG deposit. The hydrothermal

322　alteration at Alemao includes (1) Fe metasomatism leading to the formation of

323　grunerite, fayalite, and/or Fe oxides (magnetite and/or hematite), (2) intense

324　chloritization (Mg and Fe chlorite), (3) biotitization, (4) chalcopyrite and bornite, (5)

325　intense carbonate alteration (mainly siderite), and (6) local silicification and

326　tourmalinization from early to late (Barreira et al. 1999; Ronzê et al. 2000). One

327　sample contains subhedral magnetite and accessory apatite replaced by an assemblage

328　of quartz and chlorite (Fig. 2b). Magnetite is interpreted to form part of the

329　high-temperature Ca-Fe alteration facies.

330　　*Sossego:* The iron oxides in the Sossego Cu-Au deposit include magnetite and

331   ilmenite (Figs. 2c-e), and thus this deposit is classified as a magnetite-group IOCG

332   deposit. It consists of two major groups of orebodies, Sequeirinho-Pista-Baiano (SPB)

333   and Sossego-Curral (SC), with distinct types of hydrothermal alteration. The SPB

334   orebodies have undergone regional sodic alteration (albite) and later actinolite-rich

335   high-temperature Ca-Fe alteration associated with the formation of massive

336   magnetite-(apatite) bodies (Monteiro et al. 2008a, b; Xavier et al. 2012). Spatially

337   restricted zones of high-temperature K-Fe (biotite and K-feldspar) alteration overprint

338   the Ca-Fe assemblage and grade outward to chlorite-rich zones. Within the SC

339   orebodies, early albitic and subsequent high-temperature Ca-Fe alteration are poorly

340   developed, whereas the high-temperature K-Fe alteration assemblages mark the onset

341   of the mineralization and grade outward to a widespread zone of chlorite and late

342   hydrolytic low-temperature K-Fe (sericite-hematite-quartz) alteration crosscut by

343   calcite veins (Monteiro et al. 2008a, b; Xavier et al. 2012). Three samples, 080, 081,

344   and 084, are from the SC orebodies, and the other three samples, F263P, F259, and

345   SOS_39K, are from the SPB orebodies. Samples from the SC orebodies have a

346   similar mineral assemblage of magnetite, apatite, actinolite, quartz, calcite, and

347   chalcopyrite (Fig. 2c). Magnetite is anhedral to subhedral and is associated with

348   apatite and chalcopyrite. Samples from the SPB orebodies are composed of magnetite,

349   apatite, actinolite, and chalcopyrite (Fig. 2d). Some magnetite grains have exsolution

350   lamellae of rutile and ilmenite (Fig. 2e). All samples from the Sossego deposit are

351   grouped into the high-temperature Ca-Fe alteration type.

352   *Alvo 118:* The iron oxides in the Alvo 118 Cu-Au deposit include magnetite and

353   minor hematite (Figs. 2f, g), which classifies this deposit as a magnetite-group IOCG

354   deposit. It is hosted by mafic to felsic metavolcanic rocks and crosscutting granitoid

355   and gabbro intrusions. Several hydrothermal alteration zones formed toward the ore

356   zones: (1) poorly developed Na alteration (albite and scapolite); (2) high-temperature

357   K-Fe alteration (biotite or K-feldspar) accompanied by magnetite and silicification; (3)

358   widespread, pervasive chlorite alteration spatially associated with quartz–carbonate–

359   sulfide cemented breccia and vein stockworks (low-temperature Ca-Mg); and (4) local

360   post-ore quartz–sericite alteration (Torresi et al. 2012; Xavier et al. 2012). One sample

361   (AF443) from the Alvo 118 deposit is composed of magnetite, hematite, chalcopyrite,

362   chlorite, and quartz (Figs. 2f, g). Magnetite is subhedral to euhedral and associated

363   with chalcopyrite. Chlorite and quartz are interstitial to magnetite and chalcopyrite

364   (Fig. 2g). Because magnetite formation was closely related to potassic minerals

365   (Torresi et al. 2012), the sample from this deposit is classified into high-temperature

366   K-Fe alteration type.

367   *Salobo:* The Salobo Cu-Au-Ag deposit is defined as a magnetite-group IOCG

368   deposit (Fig. 2h). The ore-bearing, magnetite-rich rocks are the product of strong

369   Fe-K alteration at high temperatures (550–650°C) and have been deformed and

370   mylonitized (Lindenmayer and Teixeira 1999; Requia and Fontboté 2000; Requia et al.

371   2003). The Fe-K alteration is replaced by widespread chlorite alteration (<370°C)

372   accompanied by the formation of calcite, epidote, albite, sericite, quartz, and fluorite

373   (Xavier et al. 2012). In the magnetite-rich rocks, chlorite replaces the Fe-Mg silicates

374   (almandine, biotite, and hastingsite) and was followed by formation of greenalite

17

around fayalite and grunerite associated with fluorite and uraninite (Lindenmayer and

Teixeira 1999; Requia and Fontboté 2000; Xavier et al. 2012). Four samples from this

deposit are composed of magnetite, biotite, and minor grunerite and chalcopyrite (Fig.

2h), which are attributed to the high-temperature K-Fe alteration. Magnetite occurs as

massive aggregates associated with biotite. Chalcopyrite is disseminated in biotite or

grows along the margin of magnetite (Fig. 2h).

Olympic Dam: The main iron oxide in the Olympic Dam Cu-U-Au-Ag deposit is

hematite (Fig. 2i), the archetype of hematite-group IOCG deposit (Williams 2010a).

The key hydrothermal alteration assemblages are magnetite-pyrite-fluorapatite, and

hematite-sericite-K-feldspar-chlorite-carbonate ± Fe-Cu sulfides ± U and REE

minerals (Bastrakov et al. 2007; Apukhtina et al. 2017; Kontonikas-Charos et al.

2017). These two alteration assemblages reflect the transition from early, high

temperature and reduced fluids, followed by late, low temperature, oxidized fluids,

and from sulfide to sulfate-dominated conditions of low-temperature K-Fe alteration

(Ehrig et al. 2012, 2017). Ten samples from this deposit are composed of hematite,

K-feldspar, quartz and minor chalcopyrite and rutile (Fig. 2i).

Ernest Henry: The Ernest Henry Cu-Au deposit is a typical magnetite-group IOCG

deposit (Fig. 2j; Williams 2010a). Hydrothermal alteration and mineralization is

characterized by a regional pre-ore Na and Na-Ca alteration, overprinted by a pre-ore

K-Fe-(Mn-Ba)-rich alteration that is represented by intense biotite-magnetite and

magnetite-K-feldspar assemblage, and less common K feldspar-garnet

(manganese-rich) alteration (Mark et al. 2006; Corriveau et al. 2010; Rusk et al. 2010).

K-feldspar alteration is most intense in the vicinity of copper-gold mineralization, and forms a halo extending from several hundred meters up to 2 km beyond the ore body (Mark et al. 2006). Four samples from this deposit have a similar mineral assemblage of magnetite, K-feldspar, and minor apatite, quartz, and chalcopyrite (Fig. 2j), which belong to the high-temperature K-Fe alteration.

Candelaria: The main iron oxide in the Candelaria Cu-Au-Ag deposit is magnetite (Figs. 2k, l; Williams 2010a). Alkali metasomatism is widespread in Candelaria, including sodic (albite and/or marialitic scapolite) or K-Fe (biotite and/or K-feldspar) alteration related to ore formation (Marschik and Fontboté 2001; Marschik et al. 2003). The Cu-Fe (chalcopyrite + magnetite ± hematite) ores are associated with biotite-potassium feldspar ± calcic amphibole ± epidote alteration at Candelaria (Marschik and Fontboté 2001). Ten samples were chosen in this deposit, which have a mineral assemblage of magnetite, K-feldspar, actinolite, biotite, and chalcopyrite (Figs. 2k, l) of the high-temperature K-Fe alteration type. Magnetite is subhedral to euhedral and commonly contains inclusions of actinolite, biotite, and chalcopyrite (Fig. 2l).

Kwyjibo: The iron oxide in the Kwyjibo Cu-REE-Mo-F-U-Au deposit is mainly magnetite (Figs. 3a, b). The hydrothermal alteration at Kwyjibo is characterized by widespread Ca-Fe alteration and locally important high-temperature K-Fe and Na-Ca alteration, hematitization, silicification, and late sodic alteration (Gauthier et al. 2004; Clark et al. 2005, 2010; Corriveau et al. 2007). Early Ca-Fe and K-Fe alteration with Na depletion results in vein magnetite-titanite mineralization. Late sodic alteration is

419　local and associated with sulfides. Hematite crystallized relatively early, during

420　shearing, and also at a late stage as an alteration product of magnetite. Peripherally to

421　the magnetite-rich deposits at Kwyjibo, base metal sulfides were deposited in

422　association with a strong calcic-silicate alteration. Three samples from this deposit

423　have a mineral assemblage of magnetite, K-feldspar, biotite, quartz and minor titanite

424　(Figs. 3a, b), which belong to the high-temperature K-Fe alteration.

425　*Kiruna:* The main iron oxide in the Kiruna Fe deposit is magnetite (Fig. 3c), and

426　therefore this deposit is a magnetite-group IOA deposit. Host rock alteration around

427　Fe orebodies is characterized by actinolite and biotite of the high-temperature Ca-Fe

428　alteration type (Carlon 2000). The sample from the Kiruna deposit consists of

429　magnetite, apatite, actinolite, and minor chlorite and biotite (Fig. 3c). Magnetite is

430　subhedral to euhedral and has grain size ranging from ~100 to 1000 µm.

431　*Rektorn:* The iron oxides in the Rektorn Fe deposit include magnetite and hematite

432　(Figs. 3d, e), and therefore this deposit is classified as magnetite + hematite-group

433　IOA deposit. The Rektorn Porphyry in the lowest part of hanging wall rocks is

434　strongly altered rhyolite that varies from a massive K-feldspar to a strongly silicified

435　rock containing spherulitic aggregates of K-feldspar and disseminated hematite

436　(Geijer 1910; Martinsson et al. 2016). Sericite commonly occurs as a late-stage

437　pervasive alteration in shear zones, but also occurs as patches or lenses of massive

438　sericite containing radiating aggregates of tourmaline. The sample from the Rektorn

439　deposit is composed of magnetite, hematite, apatite, and minor K-feldspar and

440　monazite and belongs to high-temperature Ca-Fe alteration (Figs. 3d, e). Magnetite is

441   anhedral and was partly or nearly wholly transformed to hematite (Fig. 3d).

442   *El Romeral:* The main iron oxide in El Romeral is magnetite (Fig. 3f), and

443   therefore this Fe deposit is classified as magnetite-group IOA deposit. The

444   hydrothermal alteration in this deposit is represented by actinolitization, chloritization,

445   argillization, and martitization (Bookstrom 1977). Magnetite deposition was

446   accompanied by pervasive actinolitization, followed by chloritization and alteration of

447   previously actinolitized diorite and phyllite. Altered rocks within and around the

448   orebodies contain magnetite, actinolite, plagioclase, diopside, clinozoisite, titanite,

449   chlorapatite, marialitic scapolite, tourmaline, chlorite, pyrite, calcite, mica, and clays

450   (Bookstrom 1977). The sample from the El Romeral deposit consists of magnetite,

451   actinolite, and minor albite (Fig. 3f), which indicates high-temperature Ca-Fe

452   alteration.

453   *Savage River:* The Savage River is a magnetite-group IOA deposit (Fig. 3g). This

454   deposit consists of several lenses of magnetite-rich ore with amphibole (dominantly

455   tremolite-actinolite), serpentine, talc, dolomite, calcite, pyrite, chlorite, albite, quartz,

456   apatite, and hematite (Green 2012). The sample from the Savage River deposit is

457   mainly composed of magnetite and serpentine (Fig. 3g). Minor chalcopyrite is

458   disseminated in magnetite. The sample is ascribed to high-temperature Ca-Fe

459   alteration based on the abundance of amphibole (Green 2012).

460   *Pilot Knob:* The iron oxides in the Pilot Knob Fe deposit include magnetite and

461   hematite (Figs. 3h, i), and thus this deposit is defined as magnetite + hematite-group

462   IOA deposit. Wall rock alteration is rare at Pilot Knob, where minor sericite replaces

albite and K-feldspar. Late-stage hydrothermal quartz veins containing chlorite and epidote, and orthoclase veins cut the ore (Nold et al. 2013). The dominant gangue minerals are albitic plagioclase, K-feldspar, quartz, and chlorite. The sample is composed of magnetite, hematite, apatite, chlorite, and quartz (Figs. 3h, i), which belongs to the high-temperature Ca-Fe alteration.

Pea Ridge: The iron oxides in the Pea Ridge Fe deposit are mainly magnetite and hematite (Figs. 3j, k), and thus this deposit is classified as magnetite + hematite-group IOA deposit. Alteration at Pea Ridge includes silicification, potassic metasomatism and alteration of the host rocks to actinolite, chlorite, epidote, and garnet (Nuelle et al. 1992; Day et al. 2016). The amphibole-quartz zone represents the earliest phase of alteration related to ore formation. Specular hematite is partly the result of replacement of magnetite. During and after the development of specularite, a massive silicified zone forms by filling empty spaces and the replacement of the host rock. The K-Fe (K-feldspar and magnetite) alteration and sericitization (sericite and hematite) accompany silicification. The sample from the Pea Ridge deposit consists of magnetite, hematite, apatite, quartz, and minor pyrite, biotite and monazite and belongs to the high-temperature Ca-Fe alteration (Figs. 3j, k).

Lyon Mountain: The main iron oxides in the Lyon Mountain deposit are magnetite and hematite (Fig. 3l), and thus belongs to the magnetite + hematite-group IOA deposit type. The main Fe mineralization is characterized by "skarn-like" clinopyroxene-magnetite ± apatite assemblages associated with migmatization and mylonitization and occasionally potassic alteration (McLelland et al. 2002; Valley et

485 al. 2010). Two samples from Lyon Mountain are composed of magnetite, albite,

486 apatite, and minor K-feldspar and quartz (Fig. 3l), which belong to the

487 high-temperature Ca-Fe alteration.

488

489 **Average trace element composition of iron oxides**

490 A total of 521 spot analyses by EPMA and 124 line analyses by LA-ICP-MS were

491 obtained on 50 sections (Online Resource 2). Full analytical results of EPMA and

492 LA-ICP-MS are shown in Online Resources 3 and 4. Figures in Online Resources 5

493 and 6 display the chemical composition of individual analyses and average

494 composition of each sample, normalized to bulk continental crust, whereas Fig. 4

495 provides the average composition of individual deposits, normalized to bulk

496 continental crust. EPMA data show that samples from the same deposit have similar

497 normalized trace element patterns and that normalized ratios of a specific element

498 vary within one order of magnitude (Online Resource 5). Magnetite and hematite

499 from the same deposit have similar trace element patterns (Online Resource 5).

500 LA-ICP-MS data show that samples from the same deposit have more variable trace

501 element compositions with normalized Pb, Zr, Mo, and Sn contents variation

502 exceeding one order of magnitude (Online Resource 6). For IOCG deposits, samples

503 from the Alvo 118 deposit have lower Mg and Ti contents, whereas those from the

504 Sossego deposit have higher V and Ni contents (Figs. 4a, c). For IOA deposits,

505 samples from the Kiruna deposit have lower Ti content, whereas those from the Lyon

506 Mountain have lower V content (Figs. 4b, d). LA-ICP-MS data show that samples

507   from different IOCG deposits have Y, P, Pb, Zr, W, Ta, Nb, Mo, Sn, V, Ni, and Cr

508   contents varying between one and three orders of magnitude (Fig. 4c), whereas

509   samples from different IOA deposits have Ca, Y, Pb, Zr, W, Sc, Ta, Nb, Sn, Mg and

510   Co contents varying from one to four orders of magnitude (Fig. 4d). Samples from the

511   Pea Ridge deposit show W and Sn enrichment relative to other IOA deposits (Fig. 4d).

512   Average trace element compositions of each deposit are plotted in Ca+Al+Mn vs.

513   Ti+V and Ni/(Cr+Mn) vs. Ti+V diagrams proposed by Dupuis and Beaudoin (2011).

514   In general, LA-ICP-MS data have lower Ni/(Cr+Mn) ratios than EPMA data, which is

515   mainly due to lower detection limit for Ni and Cr (Fig. 5a). LA-ICP-MS data have

516   slightly higher Ca+Al+Mn values than EPMA data (Fig. 5b), which may be due to

517   some undetected mineral inclusions during LA-ICP-MS analysis. Most deposits have

518   LA-ICP-MS Ti+V contents slightly higher than EPMA Ti+V contents, with the

519   exception of Olympic Dam and Salobo deposits (Figs. 5a, b). The slightly higher

520   EPMA Ti+V contents than LA-ICP-MS Ti+V contents in Salobo magnetite may be

521   due to higher EPMA detection limits of these elements, whereas the higher EPMA

522   Ti+V contents (~0.23 wt%) than LA-ICP-MS Ti+V contents (~0.08 wt%) in Olympic

523   Dam hematite are due to microscopic Ti-rich mineral inclusions in sample OD2 that

524   was analyzed by EPMA but not by LA-ICP-MS. This likely explains why

525   LA-ICP-MS data from Olympic Dam plot in the IOCG field, whereas EPMA data of

526   this deposit plot between the Kiruna and Porphyry fields (Figs. 5a, b). As shown in

527   Fig. 5a, three IOCG deposits plot in the IOCG field and four IOA deposits in the

528   Kiruna field. Both EPMA and LA-ICP-MS data of Sossego plot above the Kiruna

529 field, whereas those of Kiruna, Pea Ridge, and El Romeral plot in the Porphyry field

530 (Fig. 5a). However, in the Ca+Al+Mn versus Ti+V diagram (Fig. 5b), most IOCG and

531 IOA deposits plot in the IOCG and Kiruna fields, respectively, indicating that this

532 diagram is more reliable. The exceptions are Candelaria that plots in the Porphyry

533 field, and Sossego which plots at the boundary between Porphyry and Kiruna fields.

534

535 **Chemical composition of iron oxides from different deposit and alteration types**

536 The minimum, maximum, median, and average trace element contents of iron oxides

537 from different deposit and alteration types are shown in Fig. 6. EPMA analyses show

538 that iron oxides from different subtypes of IOCG and IOA deposits have different

539 trace element concentrations. Iron oxides from the hematite-group IOCG deposits

540 have relatively high Si, Ca, Al, Sn, Cu, and Ti contents but low Mn, Mg, V, and Ni

541 contents, whereas those from the magnetite-group IOCG deposits are characterized by

542 relatively high Mn contents (Fig. 6a). Iron oxides from the magnetite-group IOA

543 deposits have relatively high Mg, Zn, V, and Ni contents and low Si, K, Ca, and Ti

544 contents, whereas those from the magnetite + hematite-group IOA deposits are

545 characterized by relatively high Ti but low Al contents (Fig. 6a). LA-ICP-MS analyses

546 show that magnetite-group IOCG deposits are characterized by relatively low Pb, Zr,

547 and Sc and high Ga, Mn, Zn, Ni, and Cr, whereas those from the hematite-group

548 IOCG deposits are characterized by high Si, Ca, Pb, Zr, W, Sn, Nb, Cu, and Mo but

549 low Ga, Mn, Mg, Ti, Co, V, Ni, and Cr (Fig. 6b). Iron oxides from the

550 magnetite-group IOA deposits have relatively high Mg, Co, and V contents and low Si,

551   Ca, W, Sn, Nb, and Mo contents, whereas those from the magnetite + hematite-group

552   IOA deposits have relatively high W, Sc, and Ti contents but low Al, Mg, and Zn

553   contents (Fig. 6b).

554   EPMA analyses show that iron oxides from the high-temperature Ca-Fe alteration

555   have relatively high Mg, V and Ni contents, but relatively low K and Al contents (Fig.

556   6c). Iron oxides from high-temperature K-Fe alteration have relatively high Mn and

557   Cr contents, whereas those from low-temperature K-Fe alteration have relatively high

558   Si, Ca, Sn, Cu, and Ti contents but relatively low Mn, Mg, V and Ni contents (Fig. 6c).

559   LA-ICP-MS analyses show that iron oxides from high-temperature Ca-Fe alteration

560   have relatively high Mg, Ti, Co, V, and Ni contents and low Ca, Al, Ge, Sn, Cu, and

561   Mo contents (Fig. 6d). Iron oxides from high-temperature K-Fe alteration have

562   relatively high Mn, Zn, and Cr contents but low Zr, W, and Nb contents, whereas

563   those from the low-temperature K-Fe alteration have relatively high Si, Ca, Pb, Zr, W,

564   Sn, Nb, Cu, and Mo contents but low Ga, Mn, Mg, Ti, Co, V, Ni, and Cr contents (Fig.

565   6d).

566

567   **PLS-DA results of iron oxide composition**

568   Host rocks

569   The studied deposits are divided into three groups according to the types of host rocks,

570   volcano-sedimentary rocks, volcanic rocks, and granitic rocks (Online Resource 1).

571   Figure 7 shows the PLS-DA results of EPMA and LA-ICP-MS data of iron oxides

572   classified by different host rocks. PLS-DA of iron oxide EPMA data shows that

573   despite forming overlapping clusters in t_1-t_2, samples hosted by granitic rocks plot in

574   the right side of t_1 due to correlated Si, Ti, and Al and inversely correlated to V (Figs.

575   7a, b). Iron oxides hosted by volcanic rocks are discriminated by correlated V and Mn

576   from those hosted by volcano-sedimentary rocks that show Mg and Si covariation

577   (Figs. 7a, b). The overlapping of iron oxide compositions divided by types of rocks in

578   t_1-t_2 (Fig. 7b) indicates that EPMA Si, Ca, Mg, Mn, Al, Ti, and V values are poor

579   discriminators for host rocks. PLS-DA of LA-ICP-MS data shows that samples with

580   more elemental variables result in better separation of iron oxides from different host

581   rocks. Samples hosted by granitic rocks are characterized by correlated Pb, Ge, Sn,

582   Cu, Mn, and Zn (Fig. 7c) and negative t_2 values (Fig. 7d). Samples hosted by

583   volcano-sedimentary rocks plot in the negative side of t_1 due to correlated Nb, Mo, Ni

584   and Cr, whereas samples hosted by volcanic rocks plot on the positive side of t_2 due to

585   correlated Pb, Sc, Mg, Ti, and V (Figs. 7c, d).

586

587   Deposit types

588   PLS-DA of EPMA data shows that iron oxides from IOA deposits are positively

589   correlated to Mg and V, whereas those from IOCG deposits are positively correlated

590   to Si and Al (Figs. 8a, b). IOCG and IOA deposits can be separated in the t_1-t_2 space

591   by Si, Ca, Al, Mn, Mg, Ti, Co, and Ni compositions of iron oxides (Fig. 8b). However,

592   nearly half of IOCG and IOA iron oxide compositions overlap (Fig. 8b) indicating

593   that PLS-DA of EPMA data has limited efficiency in discriminating these two deposit

594   types. In contrast, PLS-DA of LA-ICP-MS data shows that iron oxides from the IOA

595   deposits can be separated from IOCG deposits with slight overlapping due to

596   covariation of Pb, Sc, and V (Figs. 8c, d). Score contribution diagrams for both EPMA

597   (Figs. 8e, f) and LA-ICP-MS (Figs. 8g, h) data show that distinct, opposite chemical

598   signatures separate iron oxides from IOCG deposits from those from IOA deposits.

599   The score contribution plots show that positive contribution of Al, Ge, Si, Nb, Cu, Mo,

600   Ga, and Zn discriminates iron oxides from the IOCG deposits, whereas positive

601   contribution of Pb, Sc, V, and Mg discriminates those from the IOA deposits (Figs.

602   8e-g).

603   PLS-DA of EPMA data shows that iron oxides from hematite-group IOCG deposits

604   plot in the left side of t_1-t_2 because of correlated Ca, Ti, and Si, whereas those from

605   magnetite-group IOA deposits plot in the right side of t_1-t_2 due to covariation of Mg

606   and V (Figs. 9a, b). Iron oxides from magnetite + hematite-group IOA deposits are

607   near the center of the scores plot and thus are not well classified (Fig. 9b). Although

608   samples from the magnetite-group IOCG deposits are dispersed in t_1-t_2, their

609   distribution indicates that they are positively correlated to Al and Mn and negatively

610   correlated to V and Mg (Figs. 9a, b). Therefore, PLS-DA of EPMA data efficiently

611   discriminate magnetite-group IOA deposits from other types of deposits, but cannot

612   discriminate magnetite + hematite-group IOA, magnetite-group and hematite-group

613   IOCG deposits. The classification of iron oxide groups from different IOCG and IOA

614   deposits is improved by PLS-DA of LA-ICP-MS data since more elements are used

615   (Figs. 9c, d). Iron oxides from hematite-group IOCG deposits plot in the negative t_1

616   and t_2 region due to covariation of Nb, Cu, Mo, W, and Sn, whereas those from

617   magnetite + hematite-group IOA deposits plot in the negative t_1, positive t_2 region,

618   due to covariation of Sc, Pb, and Zr (Figs. 9c, d). Iron oxides from hematite-group

619   IOCG deposits can be separated from those of magnetite + hematite-group IOA

620   deposits and magnetite-group IOA deposits by t_2 (Fig. 9d). Iron oxides from

621   magnetite-group IOA deposits plot in the high, positive t_1 side due to covariations of

622   Pb and V (Fig. 9d). Iron oxides from magnetite-group IOCG deposits show a diverse

623   composition and overlap the field of magnetite-group IOA deposits (Fig. 9d). VIP plot

624   for PLS-DA of EPMA data in Fig. 9b indicates that Si, Mg, and V are important

625   elements discriminating hematite-group IOCG deposits and magnetite-group IOA

626   deposits (Fig. 9e). Aluminum and Ti are the most important elements to distinguish

627   between magnetite + hematite-group IOA deposits, whereas Mn is the important

628   element for discriminating magnetite-group IOCG deposits (Fig. 9e). The VIP

629   diagram for PLS-DA of LA-ICP-MS data in Fig. 9d indicates that Pb and Ti are

630   important factors discriminating all the deposit subtypes (Fig. 9f). In separation of

631   hematite-group IOCG deposits, Sn, Ga, Mn, and Ni are the most important, whereas

632   Al and Sc are important for other three deposit subtypes (Fig. 9f). Tungsten, Nb, Cr

633   are important variables discriminating hematite-group IOCG deposits and

634   magnetite-group IOCG deposits (Fig. 9f).

635

636   Alteration types

637   PLS-DA of EPMA data (Figs. 10a, b) shows that iron oxides formed by

638   high-temperature and low-temperature K-Fe alteration are separated by $qw*_1$ from

those formed by high-temperature Ca-Fe alteration (Fig. 10a). Despite the formation

of overlapping clusters in Fig. 10b, iron oxides from high-temperature Ca-Fe

alteration mostly plot in the high t_1 region because of correlated Mg and V, whereas

those from low-temperature K-Fe alteration have negative t_1 values due to covariation

of Si, Ca and Ti (Figs. 10a, b). Variation in Mn, Si and Ti compositions of iron oxides

separate high- and low-temperature K-Fe alteration classes (Fig. 10a). In comparison

with the EPMA data, PLS-DA of LA-ICP-MS data results in a better classification of

samples of various alteration types (Fig. 10b). This is likely due to the larger number

of LA-ICP-MS variables. Samples from the high-temperature Ca-Fe alteration are

characterized by covariation of V and Ni (Fig. 10c) and plot in the positive t_1 and t_2

region (Fig. 10d), whereas low-temperature K-Fe alteration shows correlated Nb, W,

and Zr (Fig. 10c) and plot in the positive t_1 and negative t_2 region (Fig. 10d). Samples

from high-temperature K-Fe alteration plot in the negative t_2 side due to correlated

Mn, Ge, Cr, and Zn (Figs. 10c, d). The VIP plot for PLS-DA of EPMA data in Fig.

10a indicates that Mn and V are the most important elements in the classification of

all classes (Fig. 10e). The VIP plot for PLS-DA of LA-ICP-MS data shows that V and

Ni are main contributors in separation of different sample classes in Fig. 10d.

Germanium, W, Mn, and Zn are discriminants for both high-temperature Ca-Fe and

K-Fe alteration (Fig. 10f), whereas Pb, Sn, Nb, Mo, and Ti are the most important

elements in the classification of low-temperature K-Fe alteration (Fig. 10f).

Discussion

661   Magnetite and hematite from IOCG and IOA deposits contain minor and trace

662   elements from below detection limit to a few percent. These elements are structurally

663   incorporated into magnetite/hematite or form micrometer to nanometer mineral

664   inclusions (Lindsley 1976; Wechsler et al. 1984; Huberty et al. 2012; Xu et al. 2014;

665   Nadoll et al. 2014; Deditius et al. 2018). Magnetite has an inverse spinel structure

666   with the general formula AB_2O_4, where A is divalent and B is trivalent. Nadoll et al.

667   (2014) summarized common cations that can substitute for Fe^{3+} in the tetrahedral sites

668   and Fe^{2+}/Fe^{3+} in the octahedral sites according to Goldschmidt's rule (Goldschmidt

669   1958). They suggested that Mg, Mn, Zn, Co, and Ni may substitute for Fe^{2+}, whereas

670   Al, Ga, and As substitute for Fe^{3+} (Nadoll et al. 2014). Tetravalent ions such as Ti^{4+}

671   may occupy the Fe^{3+} site by coupled substitution with a divalent cation (Wechsler et

672   al. 1984). Vanadium, Cr, and Mn have different valences, and their incorporation

673   depends on oxygen fugacity (Lindsley1976; Sievwright et al. 2017; Sossi et al. 2018).

674   Relatively high trace element contents in zoned magnetite from the Los Colorados

675   IOA deposit have been shown to contain micrometer to nanometer mineral inclusions

676   (Deditius et al. 2018). Nanometer-scale particles in trace element-rich zones are

677   caused by local mineral supersaturation in hydrothermal fluids during crystallization

678   of host magnetite (Deditius et al. 2018). If the inclusions formed under equilibrium

679   conditions, then the micrometer-scale domains sampled by EPMA and LA-ICP-MS

680   should provide information about the fluid composition. In contrast, if inclusions

681   formed under disequilibrium conditions, then large variations in trace element

682   contents are expected to characterize the iron oxide composition measured by EPMA

683 and LA-ICP-MS.

684   Iron oxide trace element composition of IOCG (Carew 2004; Rusk et al. 2009,

685 2010; Dupuis and Beaudoin 2011; Zhang et al. 2011; Acosta-Góngora et al. 2014;

686 Chen et al. 2015; De Toni 2016) and IOA (Müller et al. 2003; Knipping et al. 2015a, b;

687 Heidarian et al. 2016; Velasco et al. 2016; Broughm et al. 2017) deposits have been

688 reported. In most studies, the trace element composition of iron oxides is used to

689 discuss the factors controlling compositional variations and the formation of

690 mineralization. In addition, based on compositional differences between ore-related

691 and barren magnetite, it can be used as an indicator mineral in the exploration for

692 IOCG deposits (Carew 2004; Rusk et al. 2009, 2010; Acosta-Góngora et al. 2014).

693 Dupuis and Beaudoin (2011) investigated trace element compositions of magnetite

694 and hematite from ten IOCG and seven IOA deposits using EPMA and constructed

695 binary diagrams to discriminate these deposit types. However, due to the detection

696 limits of EPMA, several trace elements in magnetite and hematite could not be

697 measured. Moreover, some magnetite in IOA deposits experienced reequilibration

698 processes, complicating the application of these discrimination diagrams (Heidarian et

699 al. 2016; Broughm et al. 2017). Acosta-Góngora et al. (2014) and De Toni (2016)

700 linked trace element data of magnetite from IOCG deposits in the Great Bear

701 magmatic zone (Canada) to IOCG alteration types. However, due to limited data and

702 alteration types, the relationship between magnetite chemistry and alteration types

703 needs further constraints. Thus, this study combines EPMA and LA-ICP-MS data of

704 magnetite and hematite from worldwide IOCG and IOA deposits to discuss the

705 controlling factors of the iron oxide chemistry and its relationship to alteration types

706 and IOCG and IOA deposit subtypes.

707

708 **Comparison of magnetite and hematite composition**

709 For most IOCG and IOA deposits, magnetite is commonly replaced by hematite to

710 form martite, whereas the replacement of hematite by magnetite (mushketovite) is less

711 common. It has been shown that most spinel-forming elements, except Mg, are

712 retained during martitization under moderate-temperature hydrothermal oxidation

713 (Sidhu et al. 1981; Angerer et al. 2012). However, Cornell and Schwertmann (2003)

714 showed that the martitization process can expel divalent cations due to their

715 incompatible valency and ionic radii. The reduction of hematite to magnetite involves

716 reductive dissolution of hematite iron to $Fe^{2+}_{(aq)}$ followed by non-redox reaction of

717 hematite and $Fe^{2+}_{(aq)}$ to magnetite in low temperature (100-250°C) hydrothermal

718 systems (Ohmoto 2003; Otake et al. 2010). In high-temperature hydrothermal

719 environment (350-570°C), hematite can be transformed to magnetite via reductive

720 dissolution of hematite by hydrogen or iron metal (Matthews 1976). Magnetite and

721 hematite from IOA deposits, Rektorn, Pea Ridge, Pilot Knob, and Lyon Mountain,

722 show similar bulk continental crust normalized trace element patterns (Online

723 Resource 6). This indicates that magnetite and hematite in a deposit share the same

724 origin. Oxygen fugacity-sensitive elements, such as V, also show indistinguishable

725 concentrations between magnetite and hematite from these deposits (Online Resource

726 6), implying relatively stable oxygen fugacity conditions or transformation of

727 magnetite-hematite by non-redox reactions (Swann and Tighe 1977; Ohmoto 2003).

728 This conclusion is similar to previous results showing no systematic variations in

729 trace element composition between magnetite and hematite at a deposit scale (Dupuis

730 and Beaudoin 2011; Huang et al. 2015b). Considering the similar chemical

731 composition of magnetite and hematite in a deposit, they are discussed together

732 thereafter.

733

734 **Effect of oxygen fugacity and temperature on iron oxide chemistry**

735 As reviewed by Nadoll et al. (2014), various factors likely control trace element

736 incorporation in hydrothermal magnetite from different types of deposits. Although

737 there are limited studies on the partitioning of trace elements between magnetite and

738 hydrothermal fluids (Ilton and Eugster 1989), it is generally considered that the same

739 factors controlling trace elements in igneous-derived magnetite (e.g., fluid/melt

740 composition, temperature, pressure, cooling rate, oxygen fugacity, sulfur fugacity, and

741 silica activity) also control partitioning of trace elements in magnetite under high- to

742 low-temperature hydrothermal conditions, with the additional parameter of fluid-rock

743 reactions (Putnis and Austrheim 2013; Dare et al. 2014; Nadoll et al. 2014).

744 Vanadium and Sn can occur in various valency states (V^{3+}, V^{4+}, V^{5+}, Sn^{2+}, Sn^{4+}) and,

745 as such, are sensitive to oxygen fugacity in silicate melts (Goldschmidt 1958; Toplis

746 and Corgne 2002; Righter et al. 2006; Sievwright et al. 2017). For example,

747 increasing oxygen fugacity decreases the partition coefficient of V, but not of Co and

748 Ni, for magnetite in an iron-rich melt/liquid (Toplis and Corgne 2002; Righter et al.

749   2006; Sievwright et al. 2017), whereas Sn is readily partitioned into magnetite under

750   more oxidized condition (Goldschmidt 1958; Carew 2004). Carew (2004) ascribed the

751   decreasing V concentration in magnetite from K-Fe alteration to Cu-Au

752   mineralization at Ernest Henry to a progressive increase in oxygen fugacity of fluids.

753   From high-temperature Ca-Fe to K-Fe, and to low-temperature K-Fe alteration, V

754   contents in iron oxides decrease and Sn contents increase (Figs. 6c, d), which may be

755   due to the decreasing temperature and increasing oxygen fugacity during the

756   evolution of hydrothermal alteration (Corriveau et al. 2016). Moreover, iron oxides

757   from magnetite-group IOCG deposits, regarded to form at higher temperature

758   (generally >350ºC) and under relatively more reducing conditions (Williams 2010a),

759   have higher V and lower Sn contents than those from hematite-group IOCG deposits

760   (Figs. 6a, b), which are considered to have formed at lower temperature (~200-350ºC)

761   and under relatively more oxidized conditions (Williams 2010a). Similarly, iron

762   oxides from magnetite-group IOA deposits have higher V and lower Sn contents than

763   those from magnetite + hematite-group IOA deposits (Figs. 6a, b). These regular

764   variations in V and Sn contents between different deposit subtypes are most likely due

765   to the evolving oxygen fugacity and temperature of the hydrothermal systems.

766

767   **Effect of co-precipitating minerals on iron oxide chemistry**

768   Minerals co-crystallizing with iron oxides will affect their trace element composition.

769   For example, sulfide minerals preferentially incorporate chalcophile (e.g., Cu, Pb, Zn,

770   As, Ag, Sb) and siderophile elements (e.g., Ni, platinum-group elements) (Cygan and

771 Candela 1995; Fleet et al. 1996; Simon et al. 2008), whereas lithophile elements, such

772 as Mg, Al and Ti, partition into silicates (Frost 1991; Toplis and Corgne 2002). For

773 magnetite crystallized from a Fe-rich sulfide liquid, Ni, Co, Zn, Mo, Sn, and Pb have

774 lower abundance in co-precipitating magnetite because these elements partition into

775 co-crystallizing sulfides (Dare et al. 2012). Because Ni, Mo, and Co are compatible in

776 Fe-rich monosulfide solution (MSS) but incompatible in Cu-rich intermediate solid

777 solution (ISS), magnetite crystallized from MSS is depleted in these elements relative

778 to those crystallized from Cu-rich ISS in which Fe-sulfides are scarce (Dare et al.

779 2012). Such behavior is also observed within metasomatic systems. For example, at

780 the Kwyjibo deposit, magnetite (sample KJ2) associated with chalcopyrite and pyrite

781 has lower Co content, but similar Ni, than magnetite (samples KJ1, 3) associated with

782 chalcopyrite only (Online Resources 5 and 6), suggesting that co-precipitating pyrite

783 can significantly affect the Co content in magnetite. This is consistent with previous

784 conclusions of Carew (2004) and Huang et al. (2014) that the presence or absence of

785 pyrite in the mineral assemblage significantly affects the Co content, but has little

786 effect on Ni in magnetite. It is also consistent with pyrite (and arsenopyrite) in

787 mineral assemblages with Co-rich and Cu-deficient metal associations in

788 high-temperature Ca-K-Fe alteration (Corriveau et al. 2016, 2017). Compared to

789 IOCG deposits, sulfide-deficient IOA deposits iron oxides are co-precipitated with

790 minor Fe-dominant sulfides, yielding iron oxides with higher Pb and Ni contents (Figs.

791 8c, d), suggesting that Pb and Ni in IOCG iron oxides are depleted by co-precipitating

792 pyrite and/or pyrrhotite. However, the higher Cu, Mo and Zn contents in IOCG iron

793   oxides are inconsistent with partitioning in co-precipitating sulfides. This may be due

794   to the fact that the Cu-bearing sulfides tend to be paragenetically later than magnetite

795   in IOCG system (Williams et al. 2005; Zhao and Zhou 2011).

796

797   **Effect of host rocks on iron oxide chemistry**

798   The relative enrichment of Mg ± Mn in sample F392 from the Igarapé Bahia deposit,

799   sample 11CC051 from the Salobo deposit, and sample Ehenry2 from the Ernest Henry

800   deposit (Online Resource 5) could reflect differences in fluid chemistry and the

801   evolution of the alteration facies. It has been demonstrated that elements such as Mg

802   and Mn can be progressively enriched in hydrothermal fluids by extensive fluid/rock

803   interactions (Einaudi et al. 1981; Meinert et al. 2005), which is reflected in high Mg,

804   Mn, Ca and Si concentrations in skarn magnetite (Acosta-Gongora et al. 2014; Dupuis

805   and Beaudoin 2011; Nadoll et al. 2015; Zhao and Zhou 2015; Huang et al. 2016). In

806   parallel it has been demonstrated that in evolving iron oxide alkali-calcic alteration

807   systems, early skarn with high Mg is gradually replaced by the high-temperature

808   Ca-Fe alteration facie, resulting in leaching of Mg from skarn and its transfer to the

809   fluid (Corriveau et al. 2016, 2017). The varying degrees of interaction between

810   hydrothermal fluids and carbonate country rocks of skarn deposit and their subsequent

811   replacement by more evolved alteration facies can thus explain the various Mg and/or

812   Mn contents of samples in one deposit.

813   Concentrations of V, Co, Ni, and Cr in magnetite can reflect the composition of

814   host rocks and of the alteration facies (Carew 2004; Acosta-Góngora et al. 2014; Dare

815   et al. 2014; Corriveau et al. 2016, 2017). Lack of geochemical data for host rocks of

816   the studied samples prevents comparison with iron oxides compositions. The host

817   rocks have an original control on alteration facies as well as on the metal budget of

818   fluids through extensive leaching of host rocks during early albitization and

819   high-temperature Ca-Fe alteration facies (Corriveau et al. 2016, 2017), which impact

820   on iron oxide chemistry as shown by the PLS-DA results (Fig. 7). Samples hosted in

821   granitic rocks are characterized by higher Pb, Ge, Sn, Cu, Mn, and Zn contents and

822   lower V, Ni, and Cr contents (Figs. 7c, d), which is consistent with magnetite

823   precipitated from metasomatic alteration related to granitic host rocks, which has

824   elevated W, Pb, As, Mo, and Sn (Nadoll et al. 2014). Samples hosted by

825   volcano-sedimentary and volcanic rocks can be discriminated by higher V, Ni, and Cr

826   (Fig. 7d), indicating that iron oxide chemistry is partly dependent on the host rock

827   composition of systems hosting IOCG and IOA deposits.

828

829   **Relationship between deposit subtypes and iron oxide chemistry**

830   In this section, we link the chemical composition of iron oxides with deposit subtypes

831   defined by Williams (2010a). Iron oxides from different subtypes of IOCG and IOA

832   deposits have different trace element compositions. Iron oxides from the

833   hematite-group IOCG deposits are characterized by high Si, K, Ca, Al, Pb, Zr, Ge, W,

834   Sn, Sc, Nb, Cu, and Mo but low Ga, Mn, Mg, Zn, Co, V, and Ni, whereas those from

835   magnetite-group IOCG deposits have relatively low Pb, Zr, and Hf and high Ga, Mn,

836   Zn, Ni, and Cr (Figs. 6a, b). Hematite-group IOCG deposits are typically associated

837 with sericite and/or chlorite-(quartz-albite-carbonate) alteration that developed at

838 temperatures between 200 and 350°C, whereas magnetite-group IOCG deposits

839 formed in deeper crustal settings and are associated with medium to high temperature

840 (generally >350°C) silicate alteration assemblages (Williams et al. 2005; Corriveau et

841 al. 2010, 2016). The relative depletion of compatible elements (Ga, Mn, Zn, Co, Ni,

842 Cr) in hematite-group IOCG deposits iron oxides most likely results from the lower

843 temperature solubility of these elements in fluids (Nadoll et al. 2012, 2014; Dare et al.

844 2014). As discussed above, the higher Sn, and lower V, in iron oxides from the

845 hematite-group IOCG deposits are due to higher oxygen fugacity. Higher contents of

846 incompatible elements (Zr, Ge, W, Sn, Sc, Nb, Cu) in iron oxides from the

847 hematite-group IOCG deposits may partly result from reaction with granitic host

848 rocks or water/rock exchange. Iron oxides from the magnetite-group IOA deposits

849 have relatively high Mg, Co, and V and low Si, K, Ca, W, Sn, Nb, and Mo contents,

850 whereas those from magnetite + hematite-group IOA deposits have relatively high Zr,

851 W, Sn, Sc, and Ti, but low Al and Mg contents (Figs. 6a, b). The compositional

852 differences between iron oxides from magnetite-group and magnetite +

853 hematite-group IOA deposits may be also due to different temperature and oxygen

854 fugacity.

855   PLS-DA of EPMA and LA-ICP-MS iron oxide compositional data shows that

856 hematite-group IOCG deposits, magnetite-group and magnetite + hematite-group IOA

857 deposits have distinct compositional characteristics (Figs. 9b, d). Iron oxides from

858 magnetite-group IOCG deposits show a compositional diversity and overlap with

859 those from hematite-group and magnetite + hematite-group IOCG deposits (Fig. 9b).

860 Magnetite-group IOCG deposits have diverse silicate alteration assemblages,

861 including high temperature K-Fe-(Mn-Ba) and high temperature Ca-Fe-Mg-(Na)

862 (Williams 2010a). For samples in this study, magnetite-group IOCG deposits cover

863 both high-temperature K-Fe and Ca-Fe alteration types (Online Resource 2). These

864 two alteration types have different geochemical signatures (Montreuil et al. 2013;

865 Corriveau et al. 2016, 2017), which are also recorded in iron oxide composition (Figs.

866 10b, d). Therefore, the diverse chemical composition of magnetite-group IOCG

867 deposits may partly result from prograding alteration from the high-temperature

868 Ca-Fe or Ca-K-Fe to high-temperature K-Fe alteration facies.

869

870 **Relationship between alteration types and iron oxide chemistry**

871 Corriveau et al. (2010, 2016) and Montreuil et al. (2013, 2016) demonstrated that

872 each alteration type of IOCG systems in the Great Bear magmatic zone has a

873 systematic and diagnostic geochemical signature, which is largely independent of the

874 protolith. In general, K and K-Fe alteration is rich in K, Al, Ba, Si, Rb, Zr, Ta, Nb, Th

875 and U, whereas Ca-Fe alteration is rich in Ca, Fe, Mn, Mg, Zn, Ni and Co (Montreuil

876 et al. 2013). In addition, transitional alteration facies (high-temperature Ca-K-Fe,

877 skarns, and K-skarns) have been shown to have distinct mineral and metal

878 associations (Corriveau et al. 2016, 2017). In this section, we relate iron oxide

879 chemistry to IOCG alteration types defined by Corriveau et al. (2010, 2016) and

880 evaluate whether the chemical composition of magnetite can serve as a proxy of

881 geochemical signatures of hydrothermal alteration types.

882 As shown in Figs. 6c, d, iron oxides from the high-temperature Ca-Fe (including

883 some transitional high-temperature Ca-K-Fe), high-temperature K-Fe, and

884 low-temperature K-Fe alteration facies have characteristic trace element compositions.

885 The relative enrichment of Mg, Co, and Ni in iron oxides from the high-temperature

886 Ca-Fe alteration facies is consistent with the interpretation that fluids forming Ca-Fe

887 alteration are rich in Ca, Fe, Mn, Mg, Zn, Ni and Co (Montreuil et al. 2013; Corriveau

888 et al. 2016). The relative enrichment of Si, K, and Al in iron oxides from both

889 high-temperature and low-temperature K-Fe alteration is consistent with these

890 hydrothermal fluids being rich in K, Al, Ba, Si, Rb, Zr, Ta, Nb, Th and U (Montreuil

891 et al. 2013).

892 PLS-DA results of EPMA data show that iron oxides from the high-temperature

893 Ca-Fe alteration can be separated from high-temperature and low-temperature K-Fe

894 alteration due to correlated Mg and V and inversely correlated Si, Al, and Mn (Figs.

895 10a, b). This is consistent with the average trace element composition of iron oxides

896 for different types of alteration (Figs. 6c, d). Iron oxides from low-temperature K-Fe

897 alteration can be discriminated from high-temperature K-Fe alteration due to

898 correlated W, Sn, Nb, Mo and Zr (Figs. 10c, d). This indicates that trace element

899 composition of iron oxides reflect fluid composition that evolved to form various

900 alteration types.

901

902 **Relationship between IOCG and IOA deposits**

903 The relationship between IOCG and IOA deposits remains open to debate. The IOA

904 deposits were classified as a sub-type of IOCG deposits in terms of their similarities

905 in tectonic setting, association with igneous activity, mineralogy, and alteration

906 (Hitzman et al. 1992). IOCG and IOA deposits are also considered to represent

907 similar products of magmatic-hydrothermal systems derived from high-temperature

908 calc-alkaline melts variably contaminated by Fe-P-Si-rich crustal rocks and evolving

909 to A-type granites (Hitzman et al. 1992; Rhodes et al. 1999; Sillitoe and Burrows

910 2002; Corriveau et al. 2007; Tornos 2011). Based on trace element geochemistry of

911 magnetite, Broughm et al. (2017) suggested that magnetite-apatite ores at Kiruna

912 formed from hydrothermal fluids or by post-ore metamorphic or metasomatic

913 alteration. In contrast to the hydrothermal model, a magmatic model was proposed for

914 the formation of IOA deposits where magnetite was crystallized from

915 high-temperature, volatile-rich oxide melts (Nyström and Henríquez 1994; Frietsch

916 and Perdahl 1995; Henríquez and Nyström 1998; Naslund et al. 2002; Henríquez et al.

917 2003; Velasco et al. 2016). Knipping et al. (2015a, b) proposed a model for IOA

918 formation by flotation of magmatic magnetite suspensions explaining the change from

919 purely magmatic to magmatic-hydrothermal magnetite at Los Colorados (Chile), in

920 which IOA deposits are interpreted to represent the deeper roots of an Andean IOCG

921 system (Sillitoe 2003). This model is also supported by trace element geochemistry of

922 pyrite from the same deposit (Reich et al. 2016). If some authors conclude that

923 currently available data are inadequate to argue for or against a direct process link

924 between IOA and IOCG deposits (Williams 2010b), others have been able to map the

925 transition from IOA to IOCG mineralization and their associated alteration facies

926 (Mumin et al. 2010; Corriveau et al. 2016; Montreuil et al. 2016; Ehrig et al. 2017). In

927 this section, we compare trace element compositions of iron oxides between IOCG

928 and IOA deposits and investigate the possible relationship between them.

929 Magnetite-group IOCG deposits overlap to some extent with magnetite and

930 magnetite + hematite IOA deposits in the t_1-t_2 space defined by EPMA data (Fig. 9b),

931 due to the similar chemistry of their iron oxides in terms of Si, Al, Mg, Mn, Ca, V, and

932 Ti. A compositional overlap between IOCG and IOA deposits also exist for the limited

933 number of chemical variables from EPMA data (Fig. 8b). In contrast, the larger

934 number of trace elements measured by LA-ICP-MS allows discriminating IOCG from

935 IOA deposits (Figs. 8c, d). For example, samples from IOCG deposits are

936 characterized by higher Si, Al, Ge, Nb, Cu, Mo, Ga, and Zn contents, whereas those

937 from IOA deposits show higher Mg, Ti, V, Pb, and Sc contents (Figs. 8c, d). The

938 higher Ti and V contents in iron oxides from IOA compared to IOCG deposits are

939 important discrimination factors for these two types of deposits (Dupuis and Beaudoin

940 2011). Because Ti+V content in magnetite is a function of temperature and oxygen

941 fugacity (Nadoll et al. 2014, 2015), the higher Ti+V content in iron oxides from IOA

942 deposits is likely to reflect higher formation temperature and oxygen fugacity. The

943 similar alteration types (e.g., Ca-Fe alteration) and overlapping magnetite chemistry

944 between IOCG and IOA deposits (Figs. 8b, 9b, d, and 11b), are permissive evidence

945 for a genetic link between IOCG and IOA deposits despite formation under different

946 temperatures and oxygen fugacity conditions. Whether IOCG and IOA deposits

947 formed at different stages of a common magmatic or magmatic-hydrothermal system,

948 or that they formed separately, remains unresolved based on iron oxide chemistry.

949

950 **Comparison of IOCG and IOA iron oxide composition with other deposit types**

951 Makvandi et al. (2016b) showed that PLS-DA is a robust classification method to

952 distinguish the chemical composition of magnetite from different VMS settings, as

953 well as different types of mineral deposits. Iron oxides from IOCG and IOA deposits

954 overlap together in the t_1-t_2 plot (Figs. 11a, b), consistent with lack of discrimination

955 using trace elements measured by EPMA (Figs. 8a, b). IOCG and IOA deposits are

956 separated from porphyry, VMS, VMS-related BIF, and Ni-Cu sulfide deposits using

957 their iron oxide chemistry (Figs. 11b-d). Iron oxides from porphyry Cu deposits plot

958 at low t_1 values relative to IOCG deposits and IOA deposits (Fig. 11b), as a result of

959 covariation of Si, Ca, Al, Co, and Ti (Fig. 11e). Ni-Cu sulfide deposits can be

960 discriminated from other types of deposits due to positive t_2 from correlated Ni and

961 inversely correlated Si, Ca, Al, Mn, Mg, Ti, Zn, and Co in magnetite (Fig. 11f). This is

962 consistent with the results of Dupuis and Beaudoin (2011) that iron oxides from

963 Ni-Cu sulfide deposits are relatively rich in Ni and Cr but depleted in Si and Mg, and

964 thus explaining why the Ni+Cr vs. Si+Mg diagram is useful to discriminate Ni-Cu

965 sulfide deposits from other types of deposits (Boutroy et al. 2014). Iron oxides from

966 VMS deposits and VMS-related BIF are separated from those from other types of

967 deposits by t_2 due to correlated Ca but inversely correlated Ni (Figs. 11g, h),

968 consistent with the results of Makvandi et al. (2016b). The VIP plot indicates that Si

and Zn are important discriminator elements for all the selected deposit types but VMS and VMS-related BIF (Fig. 11i). The relative depletion of Si and Zn in VMS and VMS-related BIF is possibly due to the strong partitioning of Si in quartz and Zn in sphalerite, co-precipitated with magnetite. Calcium is an important discriminating element for all deposit types (Fig. 11i). Aluminum is important in discriminating IOCG, porphyry, and Ni-Cu sulfide deposits, perhaps because these deposits are magma-related (Fig. 11i). Titanium is important to discriminate VMS, VMS-related BIF, and IOA deposits (Fig. 11i). Nickel is the important discriminant element for IOA, VMS deposits, and VMS-related BIF (Fig. 11i). IOA deposits are Fe-sulfide deficient compared to VMS system, such that Ni partitions in magnetite. The relative depletion of Ni in magnetite from VMS deposits and VMS-related BIF is possibly due to partitioning of Ni into pyrrhotite co-precipitating with magnetite (Makvandi et al. 2016a).

Conclusions

The trace element composition of iron oxides from IOCG and IOA deposits is controlled by oxygen fugacity, temperature, co-precipitating minerals (mainly Fe-sulfides), and host rocks particularly granitic. The iron oxide chemistry is not related to the iron oxide mineralogy (magnetite vs. hematite) in the same deposit but closely related to alteration and deposit types. The trace element composition of iron oxides can thus serve as a proxy for hydrothermal alteration and deposit types. Iron oxides from high-temperature Ca-Fe alteration can be separated from those from

991 high- and low-temperature K-Fe alteration by higher Mg and V contents, whereas iron

992 oxides from low-temperature K-Fe alteration can be discriminated from

993 high-temperature K-Fe alteration by higher W, Sn, Nb, Mo, and Zr contents. The iron

994 oxide compositions of hematite IOCG, magnetite IOA, and magnetite + hematite IOA

995 deposits can be classified, whereas magnetite IOCG deposits overlap with the three

996 other deposit subtypes. The compositional diversity of iron oxides from magnetite

997 IOCG deposits may be due to the incremental development of high-temperature

998 Ca-Fe and K-Fe alteration associated with these deposits. The overlapping chemical

999 composition of iron oxides from IOCG and IOA deposits are permissive evidence for

1000 a genetic link between them despite formation under different temperatures and

1001 oxygen fugacity conditions.

1002

1018

1019 References

1020 Acosta-Góngora P, Gleeson S, Samson I, Ootes L, Corriveau L (2014) Trace element

1021   geochemistry of magnetite and its relationship to Cu-Bi-Co-Au-Ag-UW

1022   mineralization in the Great Bear magmatic zone, NWT, Canada. Econ Geol

1023   109:1901-1928

1024 Aitchison J (1986) The statistical analysis of compositional data. Chapman and Hall

1025   Ltd., London, UK, pp 1-416

1026 Angerer T, Hagemann SG, Danyushevsky LV (2012) Geochemical evolution of the

1027   banded iron formation-hosted high-grade iron ore system in the Koolyanobbing

1028   Greenstone Belt, Western Australia. Econ Geol 107:599-644

1029 Apukhtina OB, Kamenetsky VS, Ehrig K, Kamenetsky MB, Maas R, Thompson J,

1030   McPhie J, Ciobanu CL, Cook NJ (2017) Early, deep magnetite-fluorapatite

1031   mineralization at the Olympic Dam Cu-U-Au-Ag deposit, South Australia. Econ

1032   Geol 112:1531-1542

1033 Barnes SJ, Roeder PL (2001) The range of spinel compositions in terrestrial mafic and

1034   ultramafic rocks. J Petrol 42:2279-2302

1035   Barreira CF, Soares ADV, Ronzê PC (1999) Descoberta do depósito Cu–Au

1036   Alemão—Província Mineral de Carajás (PA). In: SBG, 6° Simpósio de Geologia

1037   da Amazônia, Manaus, AM, vol 6. Bol Res Expandidos, pp 136-139

1038   Barton MD, Johnson DA (1996) Evaporitic-source model for igneous-related Fe

1039   oxide–(REE-Cu-Au-U) mineralization. Geology 24:259-262

1040   Bastrakov EN, Skirrow RG, Davidson GJ (2007) Fluid evolution and origins of iron

1041   oxide Cu-Au prospects in the Olympic Dam district, Gawler Craton, South

1042   Australia. Econ Geol 102:1415-1440

1043   Beaudoin G, Dupuis C (2010) Iron-oxide trace element fingerprinting of mineral

1044   deposit types. In: Corriveau L, Mumin AH (eds) Exploring for iron oxide

1045   copper-gold deposits: Canada and global analogues. Geological Association of

1046   Canada, Short Course Notes 20, pp 107-121

1047   Bookstrom AA (1977) The magnetite deposits of El Romeral, Chile. Econ Geol

1048   72:1101-1130

1049   Boutroy E, Dare SAS, Beaudoin G, Barnes S-J, Lightfoot PC (2014) Magnetite

1050   composition in Ni-Cu-PGE deposits worldwide and its application to mineral

1051   exploration. J Geochem Explor 145:64-81

1052   Brereton RG, Lloyd GR (2014) Partial least squares discriminant analysis: taking the

1053   magic away. J Chemom 28:213-225

1054   Broughm SG, Hanchar JM, Tornos F, Westhues A, Attersley S (2017) Mineral

1055   chemistry of magnetite from magnetite-apatite mineralization and their host

1056   rocks: examples from Kiruna, Sweden, and El Laco, Chile. Miner Deposita

1057   52:1223-1244

1058   Buddington A, Lindsley D (1964) Iron-titanium oxide minerals and synthetic

1059   equivalents. J Petrol 5:310-357

1060   Carew MJ (2004) Controls on Cu-Au mineralisation and Fe oxide metasomatism in

1061   the Eastern Fold Belt, NW Queensland, Australia. Ph.D. thesis, James Cook

1062   University, Queensland, pp 213-277

1063   Carlon CJ (2000) Iron oxide systems and base metal mineralisation in northern

1064   Sweden. In: Porter TM (ed) Hydrothermal iron oxide copper-gold and related

1065   deposits: A global perspective, vol 1. PGC Publishing, Adelaide, pp 283-296

1066   Chen WT, Zhou M-F, Gao J-F, Hu RZ (2015) Geochemistry of magnetite from

1067   Proterozoic Fe-Cu deposits in the Kangdian metallogenic province, SW China.

1068   Miner Deposita 50:795-809

1069   Clark T, Gobeil A, Chevé S (2010) Alterations in IOCG-type and related deposits in

1070   the Manitou Lake area, eastern Grenville Province, Québec. In: Corriveau L,

1071   Mumin H (eds) Exploring for iron oxide copper-gold deposits: Canada and

1072   global analogues. Geological Association of Canada, Short Course Notes 20, pp

1073   127-146

1074   Clark T, Gobeil A, David J (2005) Iron oxide-copper-gold-type and related deposits in

1075   the Manitou Lake area, eastern Grenville Province, Quebec: variations in setting,

1076   composition, and style. Can J Earth Sci 42:1829-1847

1077   Cornell RM, Schwertmann U (2003) The iron oxides: structure, properties, reactions,

1078   occurrences and uses. John Wiley & Sons, Weinheim, pp 1-694

1079   Corriveau L, Ootes L, Mumin H, Jackson V, Bennett V, Cremer JF, Rivard B,

1080   McMartin I, Beaudoin G (2007) Alteration vectoring to IOCG(U) deposits in

1081   frontier volcano-plutonic terrains, Canada. In: Milkereit B (ed) Proceedings of

1082   Exploration 07: Fifth Decennial International Conference on Mineral Exploration.

1083   pp 1171-1177

1084   Corriveau L, Williams PJ, Mumin AH (2010) Alteration vectors to IOCG

1085   mineralization – From uncharted terranes to deposits. In: Corriveau L, Mumin H

1086   (eds) Exploring for iron oxide copper-gold deposits: Canada and global

1087   analogues. Geological Association of Canada, Short Course Notes 20, pp 89-110

1088   Corriveau L, Montreuil J-F, Potter E (2016) Alteration facies linkages among iron

1089   oxide copper-gold, iron oxide-apatite, and affiliated deposits in the Great Bear

1090   magmatic zone, Northwest Territories, Canada. Econ Geol 111:2045-2072

1091   Corriveau L, Potter EG, Acosta-Gongora P, Blein O, Montreuil J-F, De Toni AF, Day

1092   W, Slack JF, Ayuso RA, Hanes R (2017) Petrological mapping and chemical

1093   discrimination of alteration facies as vectors to IOA, IOCG, and affiliated

1094   deposits within Laurentia and beyond. Proceedings of the 14th SGA Biennial

1095   Meeting, 20-23 August 2017, Québec City, pp 851-855

1096   Cygan GL, Candela PA (1995) Preliminary study of gold partitioning among

1097   pyrrhotite, pyrite, magnetite, and chalcopyrite in gold-saturated chloride

1098   solutions at 600 to 700℃, 140 MPa, 1400 bars. In: Thompson JFH (ed) Magmas,

1099   fluids, and ore deposits, vol 23. Mineralogical Association of Canada Short

1100   Course, pp 129-137

1101 Dare SAS, Barnes S-J, Beaudoin G (2012) Variation in trace element content of

1102   magnetite crystallized from a fractionating sulfide liquid, Sudbury, Canada:

1103   Implications for provenance discrimination. Geochim Cosmochim Acta 88:27-50

1104 Dare SAS, Barnes S-J, Beaudoin G, Méric J, Boutroy E, Potvin-Doucet C (2014)

1105   Trace elements in magnetite as petrogenetic indicators. Miner Deposita

1106   49:785-796

1107 Day WC, Slack JF, Ayuso RA, Seeger CM (2016) Regional geologic and petrologic

1108   framework for iron oxide ± apatite ± rare earth element and iron oxide

1109   copper-gold deposits of the Mesoproterozoic St. Francois Mountains terrane,

1110   southeast Missouri, USA. Econ Geol 111:1825-1858

1111 Deditius AP, Reich M, Simon AC, Suvorova A, Knipping J, Roberts MP, Rubanov S,

1112   Dodd A, Saunders M (2018) Nanogeochemistry of hydrothermal magnetite.

1113   Contrib Mineral Petrol 173:46

1114 De Iorio M, Ebbels TMD, Stephens DA (2008) Statistical techniques in metabolic

1115   profiling. In: Handbook of Statistical Genetics. John Wiley & Sons, Ltd, pp

1116   347-373

1117 De Toni AF (2016) Les paragenèses à magnétite des altérations associées aux

1118   systèmes à oxydes de fer et altérations en éléments alcalins, zone magmatique du

1119   Grand lac de l'Ours. MSc thesis, Université du Québec, Institut National de la

1120   Recherche Scientifique-Centre Eau Terre Environnement, pp 1-549

1121 Dreher AM, Xavier RP, Taylor BE, Martini SL (2008) New geologic, fluid inclusion

1122   and stable isotope studies on the controversial Igarapé Bahia Cu–Au deposit,

Carajás Province, Brazil. Miner Deposita 43:161-184

Dupuis C, Beaudoin G (2011) Discriminant diagrams for iron oxide trace element fingerprinting of mineral deposit types. Miner Deposita 46:1-17

Egozcue JJ, Pawlowsky-Glahn V, Mateu-Figueras G, Barcelo-Vidal C (2003) Isometric logratio transformations for compositional data analysis. Math Geol 35:279-300

Ehrig K, Kamenetsky VS, McPhie J, Apukhtina O, Ciabanu CL, Cook N, Kontonikas-Charos A, Krneta S (2017) The IOCG-IOA Olympic Dam Cu-U-Au-Ag deposit and nearby prospects, South Australia. Proceedings of the 14th SGA Biennial Meeting, 20-23 August 2017, Québec City, pp 823-827

Ehrig K, McPhie J, Kamenetsky V (2012) Geology and mineralogical zonation of the Olympic Dam iron oxide Cu–U–Au–Ag deposit, South Australia. In: Hedenquist JW, Harris M, Camus F (eds) Geology and genesis of major copper deposits of the world. Society of Economic Geologists, Special Publication 16, Littleton, pp 237-267

Einaudi MT, Meinert LD, Newberry RJ (1981) Skarn deposits. Econ Geol 75:317-391

Eriksson L, Byrne T, Johansson E, Trygg J, Vikström C (2013) Multi- and megavariate data analysis: Basic principles and applications. MKS Umetrics AB, Sweden, pp 1-521

Fleet ME (1981) The structure of magnetite. Acta Cryst B 37:917-920

Fleet ME, Crocket JH, Stone WE (1996) Partitioning of platinum-group elements (Os, Ir, Ru, Pt, Pd) and gold between sulfide liquid and basalt melt. Geochim

1145   Cosmochim Acta 60:2397-2412

1146 Frietsch R, Perdahl J-A (1995) Rare earth elements in apatite and magnetite in

1147   Kiruna-type iron ores and some other iron ore types. Ore Geol Rev 9:489-510

1148 Frost BR (1991) Stability of oxide minerals in metamorphic rocks. Rev Mineral

1149   Geochem 25:469-488

1150 Frost BR, Lindsley DH (1991) Occurrence of iron-titanium oxides in igneous rocks.

1151   Rev Mineral Geochem 25:433-468

1152 Gauthier M, Chartrand F, Cayer A, David J (2004) The Kwyjibo Cu-REE-U-Au-Mo-F

1153   property, Quebec: a mesoproterozoic polymetallic iron oxide deposit in the

1154   northeastern Grenville Province. Econ Geol 99:1177-1196

1155 Geijer P (1910) Igneous rocks and iron ores of Kiirunavaara, Luossavaara and

1156   Tuolluvaara. Scientific and practical researches in Lapland arranged by

1157   Luossavaara-Kiirunavaara Aktiebolag. PhD Thesis, University Uppsala, Uppsala,

1158   Sweden, pp 1-278

1159 Ghiorso MS, Sack O (1991) Fe-Ti oxide geothermometry: thermodynamic

1160   formulation and the estimation of intensive variables in silicic magmas. Contrib

1161   Mineral Petrol 108:485-510

1162 Goldschmidt VM (1958) Geochemistry. Oxford University Press, London, pp 1-730

1163 Green GR (2012) Ore deposits and metallogenesis of Tasmania. Episodes 35:205-215

1164 Grigsby JD (1990) Detrital magnetite as a provenance indicator. J Sediment Res

1165   60:940-951

1166 Heidarian H, Lentz D, Alirezaei S, Peighambari S, Hall D (2016) Using the chemical

1167   analysis of magnetite to constrain various stages in the formation and genesis of

1168   the Kiruna-type chadormalu magnetite-apatite deposit, Bafq district, Central Iran.

1169   Mineral Petrol 110:927-942

1170 Helsel DR (2005) Nondetects and data analysis. Statistics for censored environmental

1171   data. Wiley-Interscience, New York, pp 1-268

1172 Henríquez F, Naslund HR, Nyström JO, Vivallo W, Aguirre R, Dobbs FM, Lledó H

1173   (2003) New field evidence bearing on the origin of the El Laco magnetite deposit,

1174   northern Chile—a discussion. Econ Geol 98:1497-1500

1175 Henríquez F, Nyström JO (1998) Magnetite bombs at El Laco volcano, Chile. GFF

1176   120:269-271

1177 Hitzman MW (2000) Iron oxide-Cu-Au deposits: what, where, when, and why. In:

1178   Porter TM (ed) Hydrothermal iron oxide copper-gold & related deposits: a global

1179   perspective, vol 1. PGC Publishing, Adelaide, pp 9-25

1180 Hitzman MW, Oreskes N, Einaudi MT (1992) Geological characteristics and tectonic

1181   setting of Proterozoic iron oxide ($Cu \pm U \pm Au \pm REE$) deposits. Precambrian

1182   Res 58:241-287

1183 Hron K, Templ M, Filzmoser P (2010) Imputation of missing values for compositional

1184   data using classical and robust methods. Computational Statistics & Data

1185   Analysis 54:3095-3107

1186 Hu H, Lentz D, Li J-W, McCarron T, Zhao X-F, Hall D (2015) Reequilibration

1187   processes in magnetite from iron skarn deposits. Econ Geol 110:1-8

1188 Huang X-W, Zhou M-F, Qi L, Gao J-F, Wang Y-W (2013) Re-Os isotopic ages of

pyrite and chemical composition of magnetite from the Cihai magmatic-hydrothermal Fe deposit, NW China. Miner Deposita 48:925-946

Huang X-W, Qi L, Meng Y-M (2014) Trace element geochemistry of magnetite from the Fe(-Cu) deposits in the Hami region, Eastern Tianshan Orogenic Belt, NW China. Acta Geol Sin 88:176-195

Huang X-W, Gao J-F, Qi L, Zhou M-F (2015a) In-situ LA-ICP-MS trace elemental analyses of magnetite and Re–Os dating of pyrite: The Tianhu hydrothermally remobilized sedimentary Fe deposit, NW China. Ore Geol Rev 65:900-916

Huang X-W, Zhou M-F, Qiu Y-Z, Qi L (2015b) In-situ LA-ICP-MS trace elemental analyses of magnetite: The Bayan Obo Fe-REE-Nb deposit, North China. Ore Geol Rev 65:884-899

Huang X-W, Gao J-F, Qi L, Meng Y-M, Wang Y-C, Dai Z-H (2016) In-situ LA-ICP-MS trace elements analysis of magnetite: The Fenghuangshan Cu-Fe-Au deposit, Tongling, Eastern China. Ore Geol Rev 72:746-759

Huang X-W, Zhou M-F, Beaudoin G, Gao J-F, Qi L, Lyu C (2018) Origin of the volcanic-hosted Yamansu Fe deposit, Eastern Tianshan, NW China: constraints from pyrite Re-Os isotopes, stable isotopes, and in situ magnetite trace elements. Miner Deposita. DOI: 10.1007/s00126-018-0794-4

Huberty JM, Konishi H, Heck PR, Fournelle JH, Valley JW, Xu H (2012) Silician magnetite from the Dales Gorge Member of the Brockman Iron Formation, Hamersley Group, Western Australia. Am Mineral 97:26-37

Ilton ES, Eugster HP (1989) Base metal exchange between magnetite and a

1211   chloride-rich hydrothermal fluid. Geochim Cosmochim Acta 53:291-301

1212 Jarosewich E, Nelen J, Norberg JA (1980) Reference samples for electron microprobe

1213   analysis. Geostand Newslett 4:43-47

1214 Knipping JL, Bilenker LD, Simon AC, Reich M, Barra F, Deditius AP, Lundstrom C,

1215   Bindeman I, Munizaga R (2015a) Giant Kiruna-type deposits form by efficient

1216   flotation of magmatic magnetite suspensions. Geology 43:591-594

1217 Knipping JL, Bilenker LD, Simon AC, Reich M, Barra F, Deditius AP, Wälle M,

1218   Heinrich CA, Holtz F, Munizaga R (2015b) Trace elements in magnetite from

1219   massive iron oxide-apatite deposits indicate a combined formation by igneous

1220   and magmatic-hydrothermal processes. Geochim Cosmochim Acta 171:15-38

1221 Kontonikas-Charos A, Ciobanu CL, Cook NJ, Ehrig K, Krneta S, Kamenetsky VS

1222   (2017) Feldspar evolution in the Roxby Downs Granite, host to Fe-oxide

1223   Cu-Au-(U) mineralisation at Olympic Dam, South Australia. Ore Geol Rev

1224   80:838-859

1225 Lee L, Helsel D (2007) Statistical analysis of water-quality data containing multiple

1226   detection limits II: S-language software for nonparametric distribution modeling

1227   and hypothesis testing. Comput Geosci 33:696-704

1228 Lindenmayer ZG, Teixeira JBG (1999) Ore genesis at the Salobo copper deposit,

1229   Serra dos Carajás. In: Silva MG, Misi A (eds) Base metal deposits of Brazil.

1230   MME/CPRM/DNPM, pp 33-43

1231 Lindsley DH (1976) The crystal chemistry and structure of oxide minerals as

1232   exemplified by the Fe-Ti oxides. In: Rumble III D (ed) Oxide Minerals. Rev.

Mineral. Mineral. Soc. Am., pp L1-L60

Liu P-P, Zhou M-F, Chen WT, Gao J-F, Huang X-W (2015) In-situ LA-ICP-MS trace

elemental analyses of magnetite: Fe–Ti–(V) oxide-bearing mafic–ultramafic

layered intrusions of the Emeishan Large Igneous Province, SW China. Ore Geol

Rev 65:853-871

Loberg BEH, Horndahl AK (1983) Ferride geochemistry of Swedish Precambrian

iron ores. Miner Deposita 18:487-504

Makvandi S, Beaudoin G, McClenaghan BM, Layton-Matthews D (2015) The surface

texture and morphology of magnetite from the Izok Lake volcanogenic massive

sulfide deposit and local glacial sediments, Nunavut, Canada: Application to

mineral exploration. J Geochem Explor 150:84-103

Makvandi S, Ghasemzadeh-Barvarz M, Beaudoin G, Grunsky EC, McClenaghan MB,

Duchesne C (2016a) Principal component analysis of magnetite composition

from volcanogenic massive sulfide deposits: Case studies from the Izok Lake

(Nunavut, Canada) and Halfmile Lake (New Brunswick, Canada) deposits. Ore

Geol Rev 72:60-85

Makvandi S, Ghasemzadeh-Barvarz M, Beaudoin G, Grunsky EC, McClenaghan MB,

Duchesne C, Boutroy E (2016b) Partial least squares-discriminant analysis of

trace element compositions of magnetite from various VMS deposit subtypes:

Application to mineral exploration. Ore Geol Rev 78:388-408

Mark G, Oliver NH, Williams PJ (2006) Mineralogical and chemical evolution of the

Ernest Henry Fe oxide–Cu–Au ore system, Cloncurry district, northwest

1255　　　　Queensland, Australia. Miner Deposita 40:769-801

1256　Marschik R, Fontboté L (2001) The Candelaria-Punta del Cobre iron oxide Cu-Au

1257　　　　(-Zn-Ag) deposits, Chile. Econ Geol 96:1799-1826

1258　Marschik R, Chiaradia M, Fontboté L (2003) Implications of Pb isotope signatures of

1259　　　　rocks and iron oxide Cu-Au ores in the Candelaria-Punta del Cobre district,

1260　　　　Chile. Miner Deposita 38:900-912

1261　Martinsson O, Billström K, Broman C, Weihed P, Wanhainen C (2016) Metallogeny

1262　　　　of the Northern Norrbotten Ore Province, northern Fennoscandian Shield with

1263　　　　emphasis on IOCG and apatite-iron ore deposits. Ore Geol Rev 78:447-492

1264　Matthews A (1976) Magnetite formation by the reduction of hematite with iron under

1265　　　　hydrothermal conditions. Am Mineral 6:927-932

1266　McLelland J, Morrison J, Selleck B, Cunningham B, Olson C, Schmidt K (2002)

1267　　　　Hydrothermal alteration of late- to post- tectonic Lyon Mountain Granitic Gneiss,

1268　　　　Adirondack Mountains, New York: Origin of quartz–sillimanite segregations,

1269　　　　quartz–albite lithologies, and associated Kiruna-type low-Ti Fe-oxide deposits. J

1270　　　　Metamorph Geol 20:175-190

1271　Meinert LD, Dipple GM, Nicolescu S (2005) World skarn deposits. In: Hedenquist

1272　　　　JW, Thompson JFH, Goldfarb RJ, Richards JP (eds) Economic Geology 100th

1273　　　　Anniversary Volume. Society of Economic Geologists, Littleton, Colorado, pp

1274　　　　299-336

1275　Monteiro LVS, Xavier RP, De Carvalho ER, Hitzman MW, Johnson CA, De Souza

1276　　　　Filho CR, Torresi I (2008a) Spatial and temporal zoning of hydrothermal

alteration and mineralization in the Sossego iron oxide–copper–gold deposit, Carajás Mineral Province, Brazil: paragenesis and stable isotope constraints. Miner Deposita 43:129-159

Monteiro LVS, Xavier RP, Hitzman MW, Juliani C, De Souza Filho CR, Carvalho EdR (2008b) Mineral chemistry of ore and hydrothermal alteration at the Sossego iron oxide–copper–gold deposit, Carajás Mineral Province, Brazil. Ore Geol Rev 34:317-336

Montreuil JF, Corriveau L, Grunsky EC (2013) Compositional data analysis of hydrothermal alteration in IOCG systems, Great Bear magmatic zone, Canada: to each alteration type its own geochemical signature. Geochem Explor Environ Anal 13:229-247

Montreuil J-F, Corriveau L, Potter E, De Toni A (2016) On the relationship between alteration facies and metal endowment of iron oxide-alkali-altered systems, southern Great Bear magmatic zone (Canada). Econ Geol 111:2139-2168

Müller B, Axelsson MD, Öhlander B (2003) Trace elements in magnetite from Kiruna, northern Sweden, as determined by LA-ICP-MS. GFF 125:1-5

Mumin AH, Somarin AK, Jones B, Corriveau L, Ootes L, Camier J (2010) The IOCG-porphyry-epithermal continuum in the Great Bear magmatic zone, Northwest Territories, Canada. In: Corriveau L, Mumin AH (eds) Exploring for iron-oxide copper-gold deposits: Canada and global analogues. Geological Association of Canada, Short Course Notes 20, pp 59-78

Nadoll P, Angerer T, Mauk JL, French D, Walshe J (2014) The chemistry of

1299   hydrothermal magnetite: A review. Ore Geol Rev 61:1-32

1300   Nadoll P, Mauk JL, Hayes TS, Koenig AE, Box SE (2012) Geochemistry of magnetite

1301   from hydrothermal ore deposits and host rocks of the Mesoproterozoic Belt

1302   Supergroup, United States. Econ Geol 107:1275-1292

1303   Nadoll P, Mauk JL, Leveille RA, Koenig AE (2015) Geochemistry of magnetite from

1304   porphyry Cu and skarn deposits in the southwestern United States. Miner

1305   Deposita 50:493-515

1306   Naslund HR, Henríquez F, Nyström JO, Vivallo W, Dobbs FM (2002) Magmatic iron

1307   ores and associated mineralization: Examples from the Chilean high Andes and

1308   coastal Cordillera. In: Porter TM (ed) Hydrothermal iron oxide copper-gold and

1309   related deposits: A global perspective, vol 2. PGC Publishing, Adelaide, pp

1310   207-226

1311   Nold JL, Davidson P, Dudley MA (2013) The pilot knob magnetite deposit in the

1312   Proterozoic St. Francois Mountains Terrane, southeast Missouri, USA: A

1313   magmatic and hydrothermal replacement iron deposit. Ore Geol Rev 53:446-469

1314   Nuelle LM, Day WC, Sidder GB, Seeger CM (1992) Geology and mineral

1315   paragenesis of the Pea Ridge iron ore mine, Washington County, Missouri-origin

1316   of the rare-earth-element-and gold-bearing breccia pipes (United States

1317   Geological Survey Bulletin 1989). In: Day WC, Lane DE (eds) Strategic and

1318   critical minerals in the Midcontinent region, United States, Chapter A. United

1319   States Government Printing Office, Washington, pp A1-A11

1320   Nyström JO, Henríquez F (1994) Magmatic features of iron ores of the Kiruna type in

Chile and Sweden; ore textures and magnetite geochemistry. Econ Geol 89:820-839

Ohmoto H (2003) Nonredox transformations of magnetite-hematite in hydrothermal systems. Econ Geol 98:157-161

Otake T, Wesolowski DJ, Anovitz LM, Allard LF, Ohmoto H (2010) Mechanisms of iron oxide transformations in hydrothermal systems. Geochim Cosmochim Acta 74:6141-6156

Putnis A, Austrheim H (2013) Mechanisms of metasomatism and metamorphism on the local mineral scale: the role of dissolution-reprecipitation during mineral re-equilibration. In: Harlov DE, Austrheim H (eds) Metasomatism and the chemical transformation of rock: The role of fluids in terrestrial and extraterrestrial processes. Springer-Verlag, Berlin-Heidelberg, pp 141-170

Ramdohr P (1980) The ore minerals and their intergrowths. Pergamon, New York, pp 1-1207

Razjigaeva N, Naumova V (1992) Trace element composition of detrital magnetite from coastal sediments of northwestern Japan Sea for provenance study. J Sediment Res 62:802-809

Reich M, Simon AC, Deditius A, Barra F, Chryssoulis S, Lagas G, Tardani D, Knipping J, Bilenker L, Sánchez-Alfaro P (2016) Trace element signature of pyrite from the Los Colorados iron oxide-apatite (IOA) deposit, Chile: a missing link between Andean IOA and iron oxide copper-gold systems? Econ Geol 111:743-761

1343   Requia K, Fontboté L (2000) The Salobo iron oxide copper-gold deposit, Carajás,

1344   northern Brazil. In: Porter TM (ed) Hydrothermal iron-oxide copper-gold and

1345   related deposits: a global perspective, vol 1. PGC Publishing, Adelaide, pp

1346   225-236

1347   Requia K, Stein H, Fontboté L, Chiaradia M (2003) Re–Os and Pb–Pb geochronology

1348   of the Archean Salobo iron oxide copper–gold deposit, Carajás mineral province,

1349   northern Brazil. Miner Deposita 38:727-738

1350   Rhodes AL, Oreskes N, Sheets SA (1999) Geology and rare earth element (REE)

1351   geochemistry of magnetite deposits at El Laco, Chile. In: Skinner BJ (ed)

1352   Geology and ore deposits of the Central Andes. Soc Econ Geol Spec Publ 7, pp

1353   299-332

1354   Righter K, Sutton SR, Newville M, Le L, Schwandt CS, Uchida H, Lavina B, Downs

1355   RT (2006) An experimental study of the oxidation state of vanadium in spinel

1356   and basaltic melt with implications for the origin of planetary basalt. Am Mineral

1357   91:1643-1656

1358   Ronzê PC, Soares ADV, dos Santos MGS, Barreira CF (2000) Alemão copper-gold

1359   (U-REE) deposit, Carajás, Brazil. In: Poter TM (ed) Hydrothermal iron oxide

1360   copper-gold & related deposits: a global perspective, vol 1. PGC Publishing,

1361   Adelaide, pp 191-202

1362   Rudnick RL, Gao S (2003) Composition of the continental crust. In: Holland HD,

1363   Turekian KK (eds) Treatise on geochemistry, vol 3. The crust. Elsevier-Pergaman,

1364   Oxford, pp 1-64

1365   Rusk B, Oliver N, Cleverley J, Blenkinsop T, Zhang D, Williams P, Habermann P

1366   (2010) Physical and chemical characteristics of the Ernest Henry iron oxide

1367   copper gold deposit, Australia; implications for IOCG genesis. In: Porter TM (ed)

1368   Hydrothermal iron oxide copper-gold & related deposits: a global perspective,

1369   vol 3. PGC Publishing, Adelaide, pp 1-18

1370   Rusk BG, Oliver NHS, Zhang D, Brown A, Lilly R, Jungmann D (2009)

1371   Compositions of magnetite and sulfides from barren and mineralized IOCG

1372   deposits in the eastern succession of the Mt Isa Inlier, Australia. In: Proceedings

1373   of GSA Annual Meeting, 18-21 October 2009, Portland. Geological Society of

1374   America Abstracts with Programs 41, pp 84

1375   Sappin A-A, Dupuis C, Beaudoin G, Pozza M, McMartin I, McClenaghan M (2014)

1376   Optimal ferromagnetic fraction in till samples along ice-flow paths: case studies

1377   from the Sue-Dianne and Thompson deposits, Canada. Geochem Explor Environ

1378   Anal 14:315-329

1379   Savard D, Barnes SJ, Dare S, Beaudoin G (2012) Improved calibration technique for

1380   magnetite analysis by LA-ICP-MS. Mineral Mag 76:2329

1381   Sidhu PS, Gilkes RJ, Posner AM (1981) Oxidation and ejection of nickel and zinc

1382   from natural and synthetic magnetites. Soil Sci Soc Am J 45:641-644

1383   Sievwright RH, Wilkinson JJ, O'Neill HSC, Berry AJ (2017) Thermodynamic

1384   controls on element partitioning between titanomagnetite and andesitic–dacitic

1385   silicate melts. Contrib Mineral Petrol 172:62

1386   Sillitoe RH (2003) Iron oxide-copper-gold deposits: an Andean view. Miner Deposita

1387   38:787-812

1388   Sillitoe RH, Burrows DR (2002) New field evidence bearing on the origin of the El

1389   Laco magnetite deposit, northern Chile. Econ Geol 97:1101-1109

1390   Simon AC, Candela PA, Piccoli PM, Mengason M, Englander L (2008) The effect of

1391   crystal-melt partitioning on the budgets of Cu, Au, and Ag. Am Mineral

1392   93:1437-1448

1393   Singoyi B, Danyushevsky L, Davidson GJ, Large R, Zaw K Determination of trace

1394   elements in magnetites from hydrothermal deposits using the LA ICP-MS

1395   technique. In: SEG Keystone Conference, Denver, USA, 2006. CD-ROM

1396   Skirrow R (2010) "Hematite-group" IOCG±U ore systems: Tectonic settings,

1397   hydrothermal characteristics, and Cu-Au and U mineralizing processes. In:

1398   Corriveau L, Mumin H (eds) Exploring for iron oxide copper-gold deposits:

1399   Canada and global analogues. Geological Association of Canada, Short Course

1400   Notes 20, pp 39-58

1401   Sossi PA, Prytulak J, O'Neill HSC (2018) Experimental calibration of vanadium

1402   partitioning and stable isotope fractionation between hydrous granitic melt and

1403   magnetite at 800°C and 0.5 GPa. Contrib Mineral Petrol 173:27

1404   Swann P, Tighe N (1977) High voltage microscopy of the reduction of hematite to

1405   magnetite. Metall Trans B 8:479-487

1406   Tallarico FH, Figueiredo BR, Groves DI, Kositcin N, McNaughton NJ, Fletcher IR,

1407   Rego JL (2005) Geology and SHRIMP U-Pb geochronology of the Igarapé Bahia

1408   deposit, Carajás copper-gold belt, Brazil: an archean (2.57 Ga) example of

1409   iron-oxide Cu-Au-(U-REE) mineralization. Econ Geol 100:7-28

1410   Tazava E, De Oliveira CG (2000) The Igarapé Bahia Au-Cu-(REE-U) deposit, Carajás

1411   Mineral Province, Northern Brazil. In: Poter TM (ed) Hydrothermal iron oxide

1412   copper–gold & related deposits: a global perspective, vol 1. PGC Publishing,

1413   Adelaide, pp 203-212

1414   Thió-Henestrosa S, Martín-Fernández J (2005) Dealing with compositional data: the

1415   freeware CoDaPack. Math Geol 37:773-793

1416   Toplis MJ, Corgne A (2002) An experimental study of element partitioning between

1417   magnetite, clinopyroxene and iron-bearing silicate liquids with particular

1418   emphasis on vanadium. Contrib Mineral Petrol 144:22-37

1419   Tornos F (2011) Magnetite-apatite and IOCG deposits formed by

1420   magmatic-hydrothermal evolution of complex calcalkaline melts. In:

1421   Proceedings of 11th Biennial SGA Meeting, 26-29 September 2011, Antofagasta,

1422   Chile, pp 443-445

1423   Tornos F, Velasco F, Hanchar JM (2016) Iron-rich melts, magmatic magnetite, and

1424   superheated hydrothermal systems: The El Laco deposit, Chile. Geology

1425   44:427-430

1426   Torresi I, Xavier RP, Bortholoto DF, Monteiro LV (2012) Hydrothermal alteration,

1427   fluid inclusions and stable isotope systematics of the Alvo 118 iron oxide–

1428   copper–gold deposit, Carajás Mineral Province (Brazil): Implications for ore

1429   genesis. Miner Deposita 47:299-323

1430   Valley PM, Fisher CM, Hanchar JM, Lam R, Tubrett M (2010) Hafnium isotopes in

zircon: A tracer of fluid-rock interaction during magnetite–apatite ("Kiruna-type") mineralization. Chem Geol 275:208-220

Velasco F, Tornos F, Hanchar JM (2016) Immiscible iron- and silica-rich melts and magnetite geochemistry at the El Laco volcano (northern Chile): Evidence for a magmatic origin for the magnetite deposits. Ore Geol Rev 79:346-366

Wechsler BA, Lindsley DH, Prewitt CT (1984) Crystal structure and cation distribution in titanomagnetites ($Fe_{3-x}Ti_x O_4$). Am Mineral 69:754-770

Whalen JB, Chappell BW (1988) Opaque mineralogy and mafic mineral chemistry of I-and S-type granites of the Lachlan fold belt, southeast Australia. Am Mineral 73:281-296

Whitten EHT (1995) Open and closed compositional data in petrology. Math Geol 27:789-806

Williams PJ (2010a) Classifying IOCG deposits. In: Corriveau L, Mumin H (eds) Exploring for iron oxide copper-gold deposits: Canada and global analogues. Geological Association of Canada, Short Course Notes 20, pp 13-22

Williams PJ (2010b) "Magnetite-group" IOCGs with special reference to Cloncurry (NW Queensland) and Northern Sweden: Settings, alteration, deposit characteristics, fluid sources, and their relationship to apatite-rich iron ores. In: Corriveau L, Mumin H (eds) Exploring for iron oxide copper-gold deposits: Canada and global analogues. Geological Association of Canada, Short Course Notes 20, pp 23-38

Williams PJ, Barton MD, Johnson DA, Fontbote L, De Haller A, Mark G, Oliver NHS,

Marschik R (2005) Iron oxide copper-gold deposits: geology, space-time distribution and possible modes of origin. In: Economic Geology 100th aniversary volume. pp 371-405

Wold S, Sjöström M, Eriksson L (2001) PLS-regression: a basic tool of chemometrics. Chemom Intell Lab Syst 58:109-130

Xavier RP, Monteiro LVS, Moreto CPN, Pestilho ALS, De Melo GHC, Da Silva MAD, Aires B, Ribeiro C, E Silva FHF (2012) The iron oxide copper-gold systems of the Carajás mineral province, Brazil. Econ Geol Spec Publ 16:433-454

Xu H, Shen Z, Konishi H (2014) Si-magnetite nano-precipitates in silician magnetite from banded iron formation: Z-contrast imaging and ab initio study. Am Mineral 99:2196-2202

Zhang D, Rusk B, Oliver N, Dai T (2011) Trace element geochemistry of magnetite from the Ernest Henry IOCG Deposit, Australia. Proceedings of 11th Biennial SGA Meeting, 26-29 September 2011, Antofagasta, Chile, pp 85-87

Zhao WW, Zhou M-F (2015) In-situ LA–ICP-MS trace elemental analyses of magnetite: The Mesozoic Tengtie skarn Fe deposit in the Nanling Range, South China. Ore Geol Rev 65:872-883

Zhao X-F, Zhou M-F (2011) Fe-Cu deposits in the Kangdian region, SW China: a Proterozoic IOCG (iron-oxide–copper–gold) metallogenic province. Miner Deposita 46:731-747

Figure captions

Fig. 1 Distribution of selected IOCG and IOA districts and related deposits. The

physical map of world is from M. Colpron (Geological Survey of Canada)

Fig. 2 Photomicrographs of ores from the IOCG deposits. All images are acquired by

back-scattered electron (BSE) imaging except one in **g** by reflected light. **a** Ore from

the Igarapé Bahia deposit (F332A) where magnetite and chalcopyrite are brecciated

and cemented by siderite. **b** Ore from the Alemao deposit (Alemao) consisting of

subhedral magnetite and accessory apatite replaced by quartz, chlorite, and minor

chalcopyrite. **c** Ore from the Sossego deposit (080) composed of euhedral to

subhedral magnetite and apatite and minor chalcopyrite cut by a quartz and calcite

assemblage. **d** Ore from the Sossego deposit (F259) composed of subhedral magnetite,

apatite, actinolite, and chalcopyrite. **e** Magnetite grains from the Sossego deposit

(SOS_39K) with exsolution lamellaes of rutile and ilmenite. Fractures of magnetite

are filled by chlorite. **f** Ore from the Alvo 118 deposit (AF443) composed of euhedral

to subhedral magnetite and chalcopyrite replaced by chlorite. **g** Part of magnetite from

the sample AF443 of the Alvo 118 deposit was transformed to hematite. **h** Ore from

the Salobo deposit (F159) composed of magnetite, biotite, and minor grunerite and

chalcopyrite. **i** Ore from the Olympic Dam (OD3) consisting of hematite, K-feldspar,

quartz and minor chalcopyrite and rutile. **j** Ore from the Ernest Henry deposit (EH1)

composed of magnetite, K-feldspar, apatite, quartz and chalcopyrite. **k** Ore from the

Candelaria deposit (LD367B) composed of magnetite, K-feldspar, actinolite, and

1496   chalcopyrite. **l** Euhedral magnetite in ore from the Candelaria deposit (Candelaria)

1497   was filled by actinolite, biotite, and chalcopyrite. Mineral abbreviation: *Ab* albite, *Act*

1498   actinolite, *Ap* apatite, *Bt* biotite, *Cal* calcite, *Ccp* chalcopyrite, *Chl* chlorite, *Ep*

1499   epidotite, *Gru* grunerite, *Hem* hematite. *Ilm* ilmenite, *Kfs* K-feldspar, *Rt* rutile, *Sd*

1500   siderite, *Ttn* titanite, *Mag* magnetite, *Qz* quartz

1501

1502   **Fig. 3** Photomicrographs of ores from the IOA deposits except **a** and **b** from IOCG

1503   deposits. **d**, **h**, and **j** are under reflected light, whereas others are BSE images. **a** Ore

1504   from the Kwyjibo deposit (KJ3) composed of subhedral to euhedral magnetite,

1505   K-feldspar, diopside, and quartz. Minor titanite and galena replaced magnetite. **b** Ore

1506   from the Kwyjibo deposit (KJ1) consisting of euhderal magnetite, K-feldspar, biotite,

1507   quartz and minor titanite. **c** Ore from the Kiruna deposit (Kiruna 1154) consisting of

1508   magnetite, apatite, actinolite, and minor chlorite and biotite. **d** Ore from the Rektorn

1509   deposit (1053) composed of magnetite, hematite, apatite, and minor K-feldspar.

1510   Magnetite was partly replaced by hematite. **e** Ore from the Rektorn deposit (1053)

1511   composed of magnetite, apatite, and monazite. **f** Ore the El Romeral deposit (El

1512   Romeral) consisting of magnetite, albite, and actinolite. **g** Ore from the Savage River

1513   deposit (Sriver) composed of magnetite, serpentine, and chalcopyrite. **h** Ore from the

1514   Pilot Knob deposit (1158) composed of magnetite and hematite. **i** Ore from the Pilot

1515   Knob deposit (1158) composed of magnetite, apatite, chlorite, and quartz. **j** Ore from

1516   the Pea Ridge deposit (1157) consisting of magnetite, hematite, and minor pyrite. **k**

1517   Ore from the Pea Ridge deposit (1157) consisting of magnetite, quartz, apatite and

1518 minor biotite and monazite. **l** Ore from the Lyon Mountain deposit (99-4A) are

1519 composed of magnetite, albite, apatite, and minor K-feldspar. Mineral abbreviation:

1520 *Ab* albite, *Act* actinolite, *Ap* apatite, *Bt* biotite, *Ccp* chalcopyrite, *Di* diopside, *Chl*

1521 chlorite, *Ga* galena, *Hem* hematite, *Kfs* K-feldspar, *Mnz* monazite, *Srp* serpentine, *Ttn*

1522 titanite, *Mag* magnetite, *Qz* quartz

1523

1524 **Fig. 4** Multi-element diagrams of average trace element composition of iron oxides

1525 from individual deposits, normalized to bulk continental crust (Rudnick and Gao

1526 2003). The light gray lines represent individual analyses. **a** and **b** EPMA data of

1527 IOCG and IOA deposits. **c** and **d** LA-ICP-MS data of IOCG and IOA deposits

1528

1529 **Fig. 5** Plot of EPMA and LA-ICP-MS data of IOCG and IOA deposits in the Ti+V vs.

1530 Ni/(Cr+Mn) (**a**) and Ti+V vs. Ca+Al+Mn (**b**) (Dupuis and Beaudoin 2011). *BIF*

1531 banded iron formation, *Skarn* Fe-Cu skarn deposits, *IOCG* iron oxide–copper–gold

1532 deposits, *Porphyry* porphyry Cu deposits, *Kiruna* Kiruna apatite-magnetite deposits.

1533 Gray line links EPMA and LA-ICP-MS average compositions for the same deposit

1534

1535 **Fig. 6** Multi-element box and whisker plots for EPMA and LA-ICP-MS trace element

1536 data of iron oxides from different deposit subtypes (**a** and **b**) and alteration types (**c**

1537 and **d**). Boxes outline the 25th to 75th percentiles and whiskers extend to the

1538 minimum and maximum values. Short line within the box represents the median value,

1539 whereas circle filled by white on the whisker represents the average value. Trace

1540 element contents below the limit of detection were removed from the box and whisker

1541 plots. Abbreviation: *HemIOCG* hematite-group IOCG deposits, *MagIOCG*

1542 magnetite-group IOCG deposits, *MagIOA* magnetite-group IOA deposits,

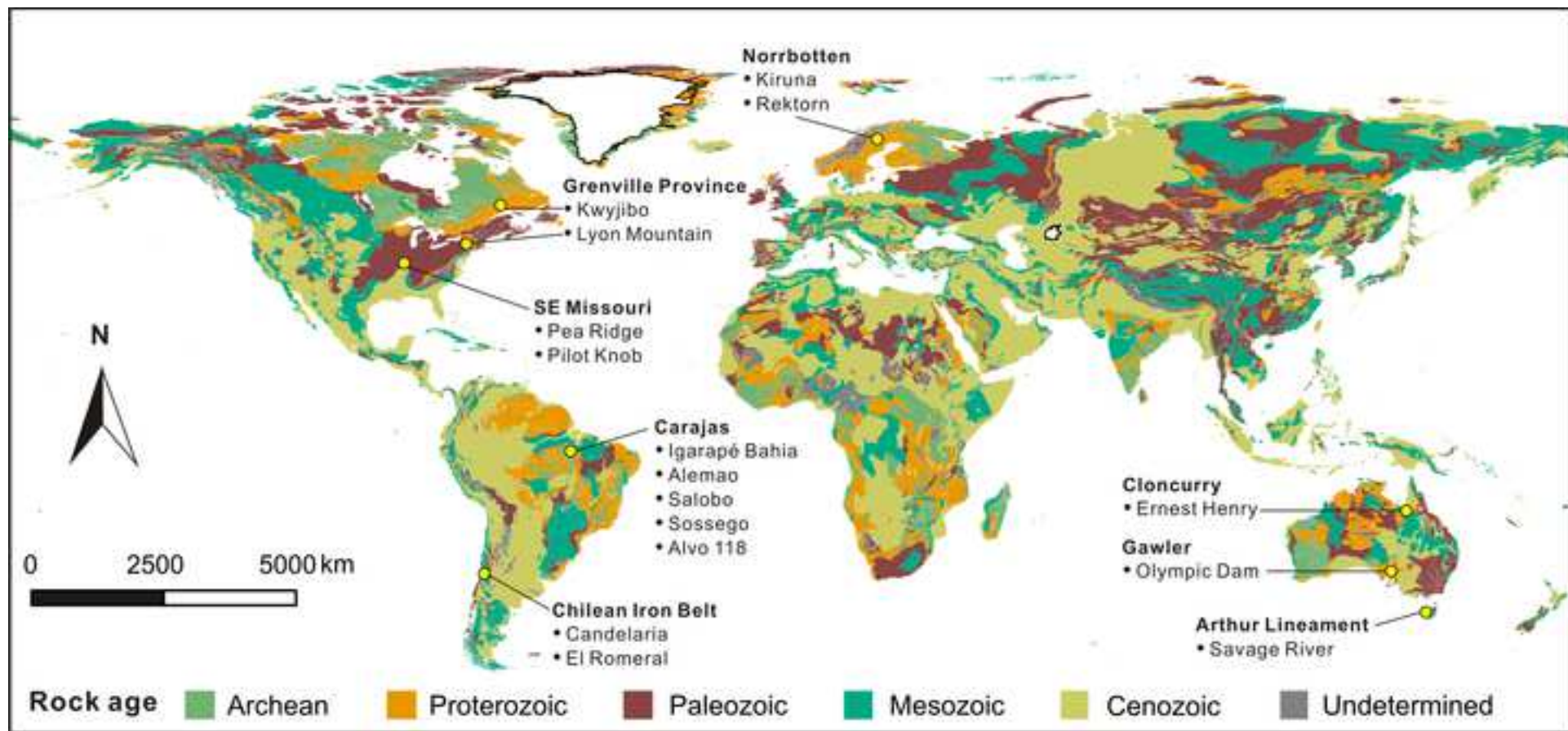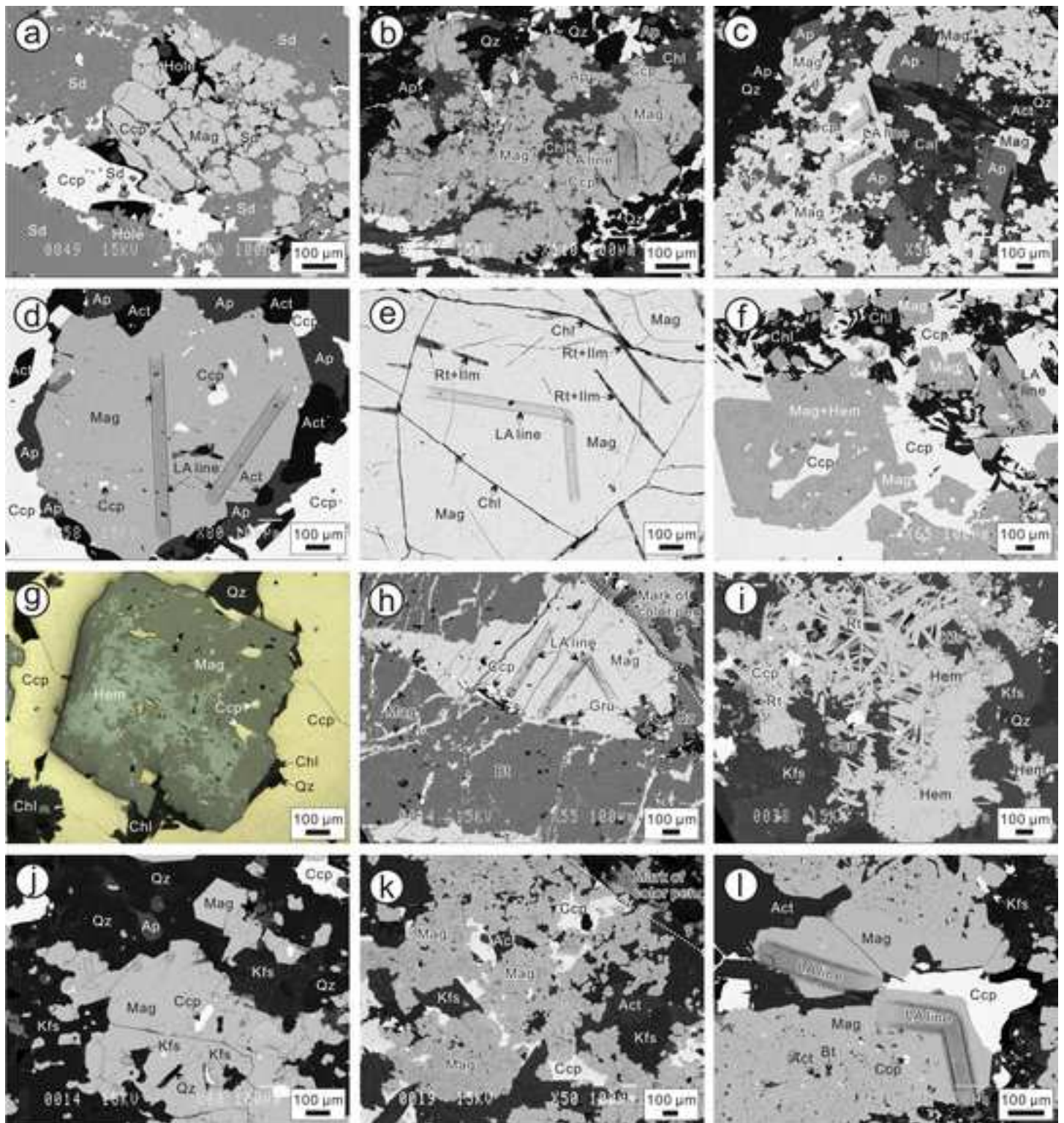1543 *MagHemIOA* magnetite + hematite-group IOA deposits, *HT Ca-Fe* high-temperature

1544 Ca-Fe alteration, *HT K-Fe* high-temperature K-Fe alteration, *LT K-Fe*
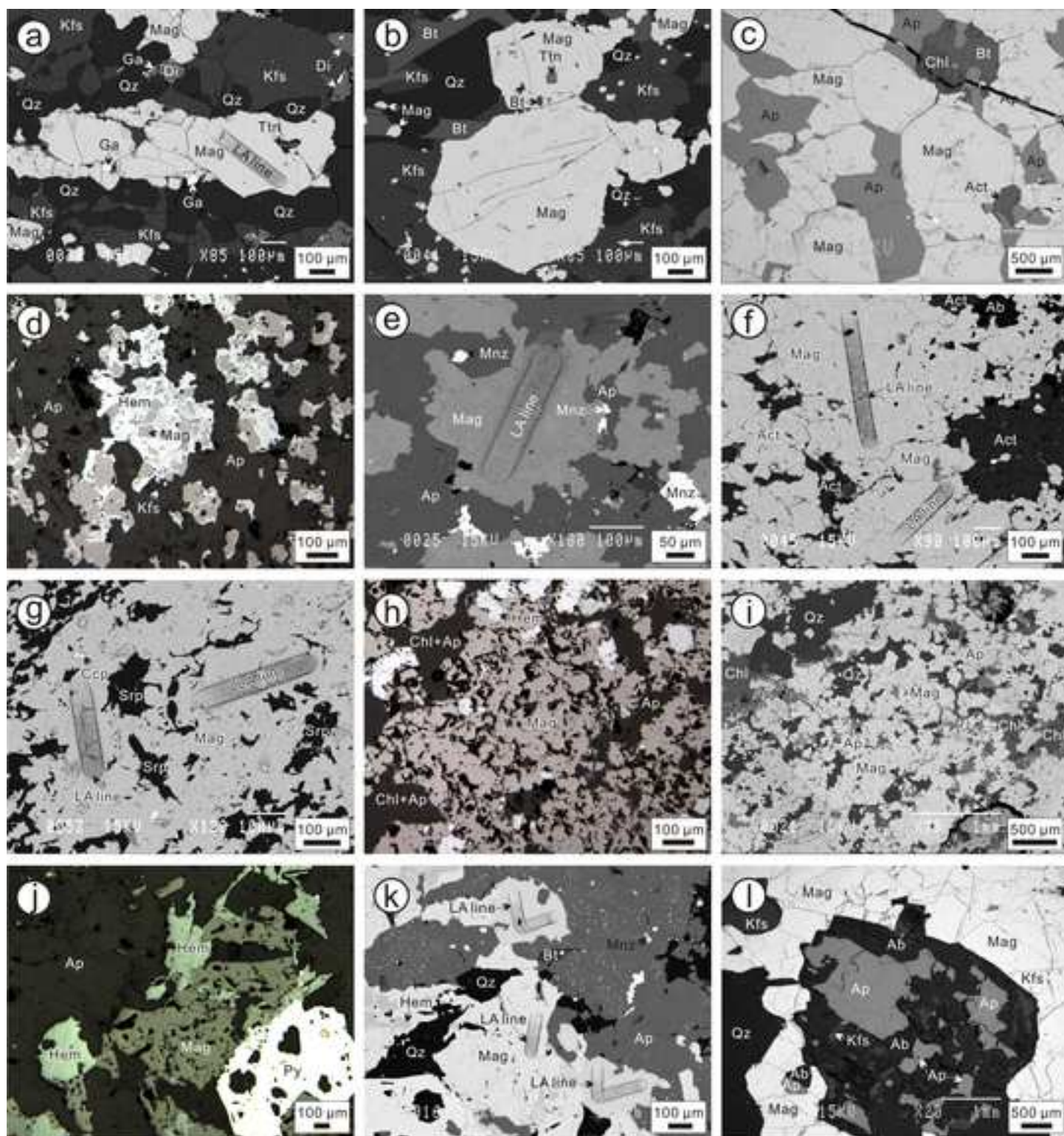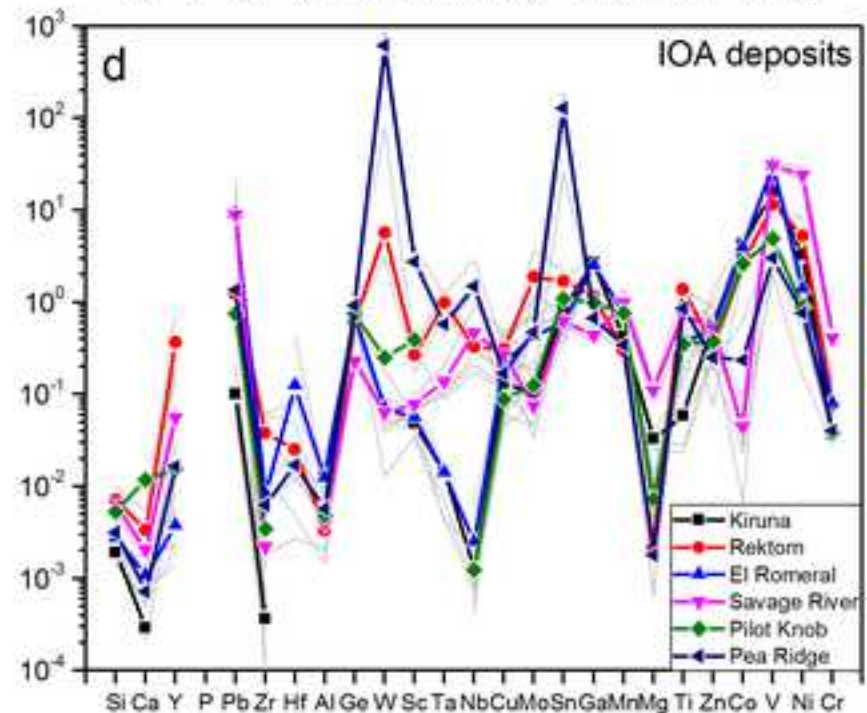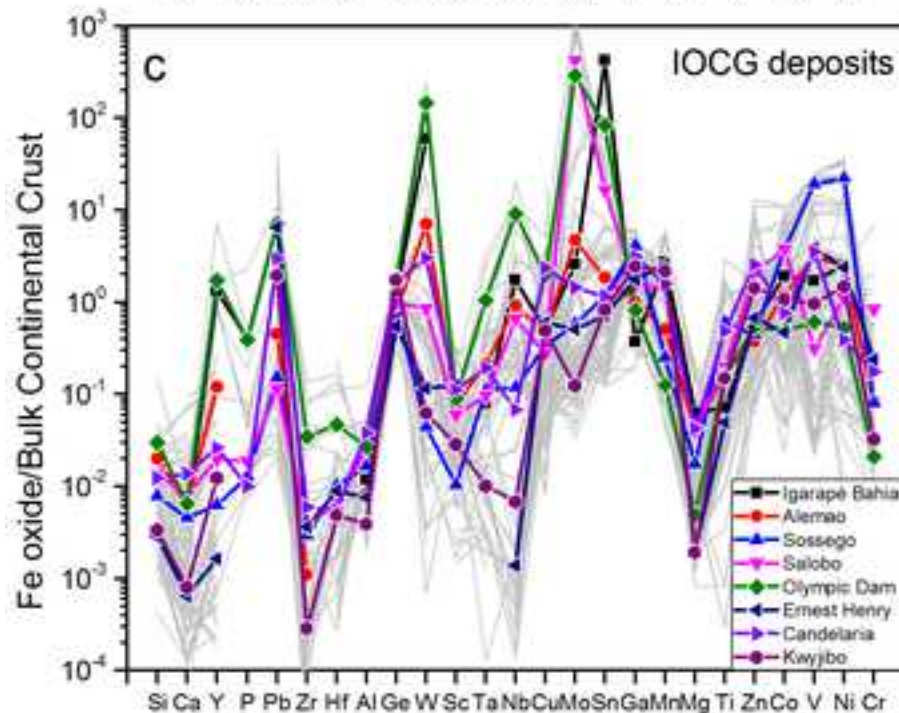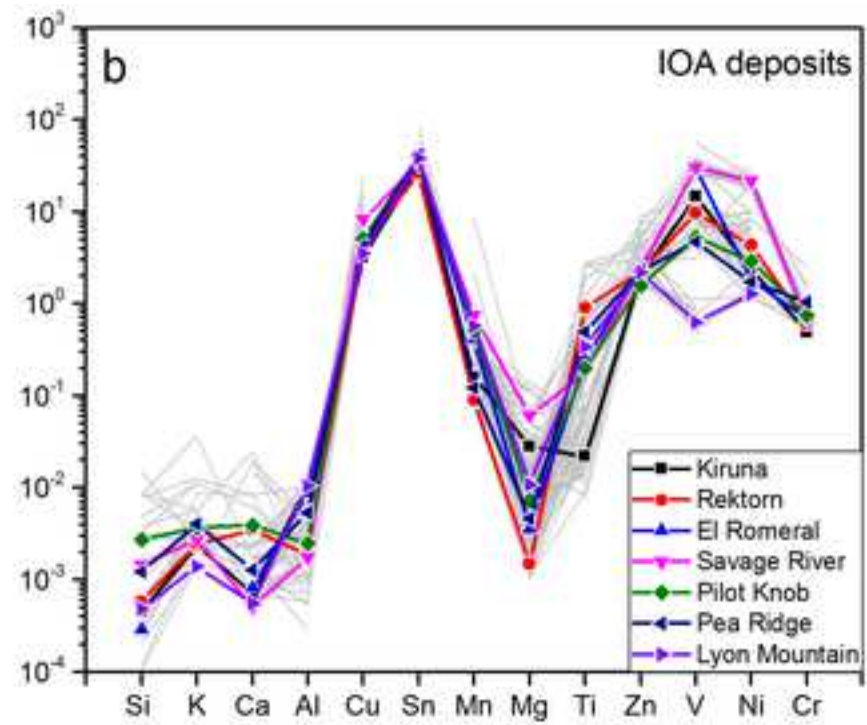
1545 low-temperature K-Fe alteration

1546

1547 **Fig. 7** PLS-DA of EPMA (**a, b**) and LA-ICP-MS (**c, d**) data of iron oxides grouped by

1548 host rocks. **a** The qw$^*_1$-qw$^*_2$ (first and second loadings) plot based on EPMA data

1549 showing correlations among element variables and host rocks. **b** The t_1-t_2 (first and

1550 second scores) plot showing the distribution of individual analyses of samples in the

1551 latent variable space defined by qw$^*_1$-qw$^*_2$ in **a**. **c** The qw$^*_1$-qw$^*_2$ (first and second

1552 loadings) plot based on LA-ICP-MS data showing correlations among element

1553 variables and host rocks. **d** The t_1-t_2 (first and second scores) plot showing the

1554 distribution of individual analyses of samples in the latent variable space defined by

1555 qw$^*_1$-qw$^*_2$ in **c**

1556

1557 **Fig. 8** PLS-DA results of EPMA and LA-ICP-MS data of iron oxides from IOCG and

1558 IOA deposits. **a** Plot of qw$^*_1$ vs. qw$^*_2$ (first and second loadings) based on EPMA

1559 data showing correlations among element variables and deposit types. **b** Plot of t_1 vs.

1560 t_2 (first and second scores) showing the distribution of individual analyses from

1561 different deposit types in the latent variable space defined by qw$^*_1$-qw$^*_2$ in **a**. **c** Plot

1562 of qw^*_1 vs. qw^*_2 (first and second loadings) based on LA-ICP-MS data showing

1563 correlations among element variables and deposit types. **d** Plot of t_1 vs. t_2 (first and

1564 second scores) showing the distribution of individual analyses from different deposit

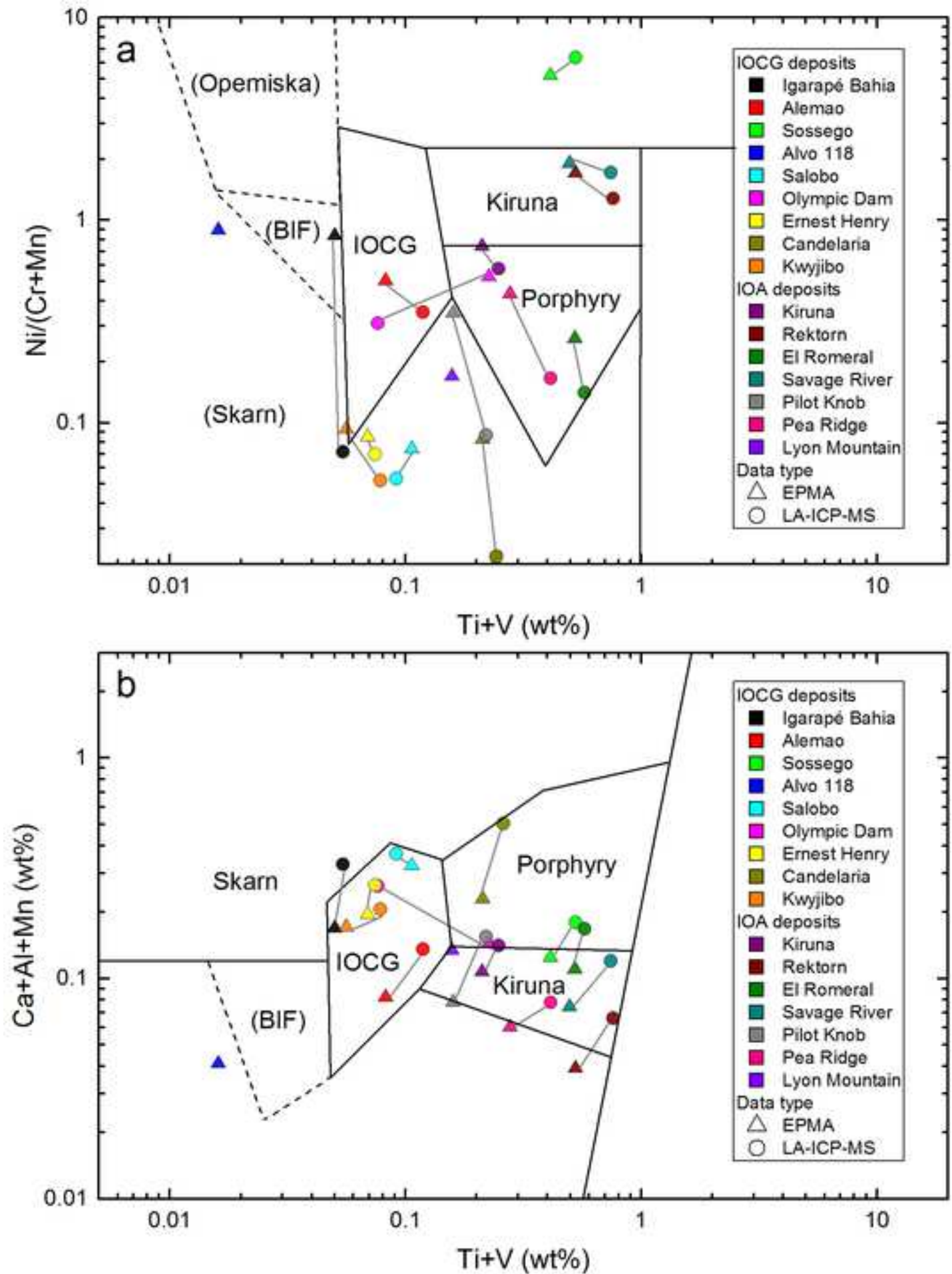1565 types in the latent variable space defined by qw^*_1-qw^*_2 in **c**. (**e-h**) Score contribution

1566 plots of elements for IOCG and IOA deposits

1567

1568 **Fig. 9** PLS-DA results of EPMA and LA-ICP-MS data of iron oxides from different

1569 subtypes of IOCG and IOA deposits. **a** Plot of qw^*_1 vs. qw^*_2 (first and second

1570 loadings) based on EPMA data showing correlations among element variables and

1571 deposit subtypes. **b** Plot of t_1 vs. t_2 (first and second scores) showing the distribution

1572 of individual analyses of samples from different deposit subtypes in the latent variable

1573 space defined by qw^*_1-qw^*_2 in **a**. **c** Plot of qw^*_1 vs. qw^*_2 (first and second loadings)

1574 based on LA-ICP-MS data showing correlations among element variables and deposit

1575 subtypes. **d** Plot of t_1 vs. t_2 (first and second scores) showing the distribution of

1576 individual analyses of samples from different deposit subtypes in the latent variable

1577 space defined by qw^*_1-qw^*_2 in **c**. **e** The VIP showing the importance of compositional

1578 variables in classification of samples in **b**. **f** The VIP showing the importance of

1579 compositional variables in classification of samples in **d**. Gray lines in **e** and **f**

1580 represent the VIP value of 1. Elements with VIP value higher than 1 are the most

1581 important in the classification. Abbreviation: *HemIOCG* hematite-group IOCG

1582 deposits, *MagIOCG* magnetite-group IOCG deposits, *MagIOA* magnetite-group IOA

1583 deposits, *MagHemIOA* magnetite + hematite-group IOA deposits

1584

Fig. 10 PLS-DA results of EPMA and LA-ICP-MS data of iron oxides from different alteration types. **a** Plot of qw*$_1$ vs. qw*$_2$ (first and second loadings) based on EPMA data showing correlations among element variables and alteration types. **b** Plot of t$_1$ vs. t$_2$ (first and second scores) showing the distribution of individual analyses of samples from different alteration types in the latent variable space defined by qw*$_1$-qw*$_2$ in **a**. **c** Plot of qw*$_1$ vs. qw*$_2$ (first and second loadings) based on LA-ICP-MS data showing correlations among element variables and alteration types. **d** Plot of t$_1$ vs. t$_2$ (first and second scores) showing the distribution of individual analyses of samples from different alteration types in the latent variable space defined by qw*$_1$-qw*$_2$ in **c**. **e** The VIP showing the importance of compositional variables in classification of samples in **b**. **f** The VIP showing the importance of compositional variables in classification of samples in **d**. Gray lines in **e** and **f** represent the VIP value of 1. Elements with VIP value higher than 1 are the most important in the classification. Abbreviation: *HT Ca-Fe* high-temperature Ca-Fe alteration, *HT K-Fe* high-temperature K-Fe alteration, *LT K-Fe* low-temperature K-Fe alteration

1600

Fig. 11 PLS-DA results of chemical composition of iron oxides from different types of deposits. **a** Plot of qw*$_1$ vs. qw*$_2$ (first and second loadings) showing correlations among element variables and deposit types. **b** Plot of t$_1$ vs. t$_2$ (first and second scores) showing the distribution of individual analyses from different deposit types in the latent variable space defined by qw*$_1$-qw*$_2$ in **a**. (**c-h**) Score contribution plots of

1606   elements for different deposit types. **i** The VIP showing the importance of

1607   compositional variables in classification of samples in **b**. Data sources: IOCG and

1608   IOA deposits (this study), Porphyry deposits (unpublished data of Huang et al.),

1609   Ni-Cu sulfide deposits (Boutroy et al. 2014), VMS deposits and VMS-related BIF

1610   (Makvandi et al. 2016a, b)

Fig. 1

Norrbotten
• Kiruna
• Rektorn

Grenville Province
• Kwyjibo
• Lyon Mountain

SE Missouri
• Pea Ridge
• Pilot Knob

Carajas
• Igarapé Bahia
• Alemao
• Salobo
• Sossego
• Alvo 118

Cloncurry
• Ernest Henry

Gawler
• Olympic Dam

Chilean Iron Belt
• Candelaria
• El Romeral

Arthur Lineament
• Savage River

N

0   2500   5000 km

Rock age   ▮ Archean   ▮ Proterozoic   ▮ Paleozoic   ▮ Mesozoic   ▮ Cenozoic   ▮ Undetermined

Fig. 2

Click here to download Figure Fig. 2.tif ⬇

Fig. 3

Fig. 4

Click here to download Figure Fig. 4.tif ⬇

Fig. 5

Click here to download Figure Fig. 5.tif ⬇

Fig. 6

Fig. 7

Fig. 8

Click here to download Figure Fig. 8.tif ⬇

Fig. 9

Fig. 10

Click here to download Figure Fig. 10.tif ⬇

Fig. 11

Click here to access/download
Supplementary Material
ESM_1.pdf

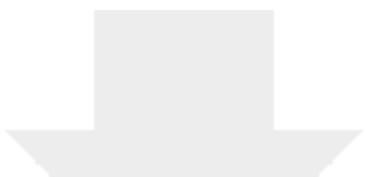Click here to access/download
Supplementary Material
ESM_2.pdf
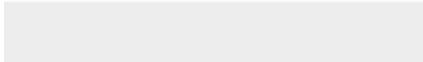
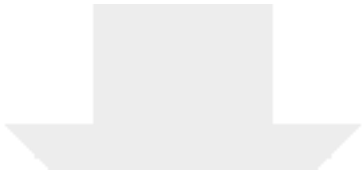Click here to access/download
Supplementary Material
ESM_3.pdf

ESM_4

Click here to access/download
Supplementary Material
ESM_4.pdf

ESM_6

Click here to access/download
Supplementary Material
ESM_6.pdf